Mush amalgamation, short residence, and sparse detectability of eruptible magma before Andean super-eruptions

G. Weber[1], J. Blundy[1], and D. Bevan[2]

[1]Department of Earth Sciences, University of Oxford, Oxford, United Kingdom.

[2]School of Earth Sciences, University of Bristol, Bristol, United Kingdom.

Corresponding author: Gregor Weber (gregor_weber@gmx.de)

Key Points:

- Sr-isotopes in plagioclase record the emergence of eruptible magma through amalgamation of pre-existing mush in the Central Andes
- The amalgamated magma did not reside at depth for longer than centuries to millennia based on diffusion chronometry
- Forward modelling indicates that high-precision gravity monitoring has large potential to resolve eruptible magma amalgamation

Abstract

Giant volcanic eruptions have the potential to overturn civilization. Yet, the driving mechanism and timescale over which batholithic magma reservoirs transition from non-eruptible crystal mush to mobile melt-dominated stages and our capacity to detect a pending super-eruption remain obscure. Here we show, using Sr isotope zonation in plagioclase crystals from three Andean large magnitude eruptions (Atana, Toconao and Tara ignimbrites), that eruptible magma has emerged by amalgamation of isotopically diverse crystal populations and silicic melt without large-scale reheating. In each case, crystals record large isotopic diversity in crystal cores, converging towards a common value in crystal rims that coincides with the composition of the rhyolitic carrier melt. Using diffusion chronometry, we constrain that the assembled eruptible magma has resided in the Earth crust for timescales of no more than decades to centuries for Atana and Tara, and up to several millennia for Toconao. These timescales and isotopic observations are consistent with the accumulation and destabilization of melt rich layers in crystal mush. While the prospect of capturing such melt lenses with most geophysical monitoring techniques is pessimistic, gravity modelling indicate that such structures are potentially resolvable. Our findings provoke a new assessment of the origin and hazards associated with large magnitude explosive eruptions.

Plain Language Summary

Super-eruptions are the largest type of explosive volcanism on Earth. If such an event would occur today, it could deeply impact human civilization. Yet, signals that may emerge prior to large explosive eruptions are difficult to constrain. To gain greater understanding of the mechanisms and timescales at which giant melt-rich reservoirs form and to evaluate our capacity of capturing the evolution towards large volcanic eruptions, we studied plagioclase crystals from three

large magnitude eruptions in the Central Andes. Using a new type of laser mass spectrometer we analyzed Sr-isotopes in traverses from crystal cores to rims, which provides a temporal record of melt composition. Our results show that in each case, the eruptible magma amalgamated from distinct pre-existing magma pockets that became merged prior to eruption. This merged state of the magma did not exist for longer than a few hundred to thousands of years based on the preservation of the crystal Sr-isotope traverses at high temperatures. These results are consistent with the accumulation and destabilization of melt-rich layers on timescales comparable to human lifespans. Although most geophysical imaging methods are unlikely to capture this process, our calculations indicate that gravity monitoring of super-volcanoes can potentially resolve such structures.

1 Introduction

Earth history is punctuated by voluminous outbursts of magma, commonly termed super-eruptions, when a dense rock volume of greater than 450 km^3 is explosively discharged to the Earth surface (Self, 2006; Wilson *et al.*, 2021; Sparks *et al.*, 2022). Such events are rare but will inevitably occur again in the future with severe consequences for life on Earth (Rampino, 2002; Self and Blake, 2008; Papale, 2018; Black et al., 2021). While several volcanoes capable of producing such eruptions have been identified, the processes and timescales over which such systems transition from dormancy to eruption are not well understood. Such information is, however, crucial to evaluate our capacity to capture the evolution towards large magnitude eruptions using geophysical monitoring techniques and constrain potential eruption harbingers.

A prerequisite to producing a supereruption is that sufficiently large volumes of eruptible magma (i.e. magma with typically <50 % crystallinity) accumulate in Earth's crust (Marsh, 1981; Vigneresse et al., 1996; Bachmann and Bergantz, 2008; Annen, 2009; Dufek and Bachmann, 2010; Caricchi et al., 2014; Barker et al., 2016). The search for such high melt fraction anomalies by geophysical methods has to date, however, been inconclusive (Magee et al., 2018), providing one of the various lines of evidence to the widely recognized notion that magmatic systems spend most of their lifespan in a crystal-rich non-eruptible state (i.e. crystal mush) (Bachmann and Bergantz, 2004, 2008; Cashman et al., 2017; Jackson et al., 2018; Bachmann and Huber, 2019; Edmonds et al., 2019). Such crystal mushes are comprised of a rigid crystal framework and interstitial melt, which due to rheological impediments are not eruptible until some melt mobilisation process takes place, the nature of which is still widely debated (Sisson and Bacon, 1999; Burgisser and Bergantz, 2011; Wotzlaw et al., 2014; Barker et al., 2016; Gualda and Sutton, 2016; Pistone et al., 2017; Rubin et al., 2017; Szymanowski et al., 2017; Spera and Bohrson, 2018).

Geochemical observations and theoretical modelling have been used to argue for both long (several hundred ka) and short (month to centuries) timescales for the transition from mush to eruptible magma. Intrusion of hot mafic magma into or beneath crystal mushes may induce melting and reduce the fraction of crystals

present in such systems, thereby increasing eruptibility. Support for this hypothesis, commonly termed 'thermal rejuvenation', has been derived from the resorption or absence of mineral phases in the erupted rock (Bachmann et al., 2002; Sliwinski et al., 2019) or in the form of time-temperature reconstructions based on zircon dating and trace element chemistry (Claiborne et al., 2010; Wotzlaw et al., 2013, 2014; Klemetti and Clynne, 2014; Tapster et al., 2016; Szymanowski et al., 2017, 2019). Thermodynamic and fluid mechanical models of thermal reactivation processes require timescales of 1000s to 10.000s of years (Huber et al., 2011; Spera and Bohrson, 2018), consistent with zircon-derived estimates, showing evidence for an evolution towards higher temperatures prior to large eruptions. However, temperature increases over such timescales may also reflect the long-term thermal maturation of magma reservoirs during their assembly, which for moderate magma fluxes will inevitably lead to increasing temperatures with time without the need of a causative rise in crustal magma injection rates (Weber et al., 2020b, 2020a; Liu et al., 2021; Lukács et al., 2021). Crystal-scale studies that employ modelling of the diffusive relaxation of elemental contents in various mineral phases, frequently find evidence for the assembly of eruptible magma on timescales of decades to centuries prior to volcanic eruptions, independent of their size (Druitt et al., 2012; Allan et al., 2013, 2017; Chamberlain et al., 2014; Cooper et al., 2017; Rubin et al., 2017; Shamloo and Till, 2019). While it has been argued that such short timescales are inconsistent with thermal rejuvenation and may reflect single magma recharge events rather than the assembly of eruptible magma (Spera and Bohrson, 2018), numerical models of the growth and destabilisation of melt-rich layers in crystal mush do not require large-scale reheating and are consistent with rapid timescales (Burgisser and Bergantz, 2011; Jackson et al., 2018; Seropian et al., 2018).

Mineral-scale reconstructions of the processes and pace of eruptible magma assembly prior to volcanic eruptions can be ambiguous due to multiple, aliased dependencies (e. g. pressure, temperature, melt chemistry, fO_2, aH_2O) that may blur the interpretation of such records. We take advantage of recent technical improvements in the capability to measure *in-situ* Sr isotope ratios in plagioclase crystals (Bevan et al., 2021), a record that is only dependent on melt isotopic composition during crystal growth and is consequently less ambiguous to interpret than simple elemental crystal zonation pattern (e.g. Tepley et al., 2000; Davidson et al., 2001, 2007; Ramos et al., 2005; Chadwick et al., 2007; Charlier et al., 2007; Waight and Tørnqvist, 2018). We show that the crystal cargo of three ignimbrite-forming eruptions from the Altiplano-Puna Volcanic Complex (Central Andes), originated from spatially and/or temporally separated magma batches that were merged by mingling with a common rhyolitic melt prior to eruption without evidence for thermal rejuvenation. Using diffusion chronometry, we estimate that the final assembled magma has resided pre-eruptively for no more than a few decades to millennia in the Earth crust. Finally, we discuss and evaluate our capacity to capture the evolution towards large magnitude eruptions using state-of-the-art geophysical methods.

2 Regional Context: Altiplano-Puna Magma Body and Ignimbrites

Recent geophysical and geodetic surveys have revealed a colossal, active magma accumulation beneath the Altiplano-Puna highland of Northern Chile and Bolivia (Fig. 1), comprising a volume of roughly 500,000 km^3 of partially molten rock with melt fraction of about 20 %, (Pritchard et al., 2018). Over the last 10 million years this area, referred to as Altiplano-Puna Volcanic Complex (APVC), has been one of the most productive volcanic regions on Earth (De Silva et al., 2006; Kay et al., 2010; Salisbury et al., 2011; Brandmeier and Wörner, 2016; Kern et al., 2016; de Silva and Kay, 2018). A direct relationship between this large magma body the Altiplano Puna Magma Body, APMB), which has been imaged by seismic, gravity and magnetotelluric techniques (Zandt et al., 2003; del Potro et al., 2013; Ward et al., 2014, 2017; Comeau et al., 2015, 2016), and extensive deposits of voluminous pyroclastic density currents (or ignimbrite) can be inferred from the juxtaposition of large silicic caldera complexes and the inferred geophysical anomaly (Fig. 1). Large scale ground deformation has been observed over the last 20 years centred at Uturuncu stratovolcano in the central part of the APVC, testifying to the active nature of the APMB (Hickey et al., 2013; Perkins et al., 2016; Gottsmann et al., 2017). In this study we reconstruct the conditions and processes leading up to three large eruptions in the APVC that span a range of bulk-rock compositions and volumes: The dacitic Atana and Tara, and rhyolitic Toconao ignimbrites.

The Atana and Toconao ignimbrites have been traced back to a source within the 60 to 35 km-wide La Pacana caldera complex in Northern Chile (Gardeweg and Ramírez, 1987; Lindsay, 2001; Lindsay et al., 2001). With an estimated dense rock equivalent (DRE) volume of 1600 km^3, the Atana ignimbrite is the most voluminous eruption known in the Central Andes (Lindsay et al., 2001; Brandmeier and Wörner, 2016), marking the peak conditions in the flare-up of large magnitude eruptions that this region has experienced over the last 10 Ma (de Silva and Gosnold, 2007; de Silva and Kay, 2018). Volume estimates for the Toconao eruption have been challenging due to limited exposure, but the preserved outflow sheet has a volume of about 180 km^3 (Lindsay et al., 2001). $^{40}Ar/^{39}Ar$ dating of biotite grains has constrained the isochrone age of the Atana eruption to 3.92±0.14 Ma (Salisbury et al., 2011). Although high precision geochronology is currently not available for the Toconao eruption, its stratigraphic position below the Atana ignimbrite, K-Ar dating and U-Pb ages of zircon crystals indicate eruption between 4.0 and 4.5 Ma (de Silva, 1989; Kern et al., 2016). Thus, these two ignimbrites could have been erupted in rapid succession. Mineral thermobarometry has been used to constrain a pre-eruptive pressure of 200 MPa and temperatures for the Atana and Toconao ignimbrites to be 770-790°C and 730–750°C, respectively (Lindsay, 2001). The pre-eruptive water contents have been determined by melt inclusion analysis and phase equilibria modelling to be 3.1-4.4 wt.% for the Atana ignimbrite and 6.3-6.8 wt.% H_2O for the Toconao magma (Lindsay, 2001). Like other Central Andean ignimbrites, initial (i.e. time-corrected) whole-rock $^{87}Sr/^{86}Sr$ compositions are highly heterogeneous for different whole-rock samples but overlapping for the Atana and Toconao eruptions within the range 0.7093-0.7131, confirming an

important petrogenetic role of crustal assimilation, in keeping with other silicic magmas of the APVC (Lindsay, 2001; Schmitt et al., 2001; Kay et al., 2010; Freymuth et al., 2015; Brandmeier and Wörner, 2016).

The dacitic Tara ignimbrite is sourced from the 20 x 30 km wide Guacha II Caldera in Bolivia, part of the larger nested Cerro Guacha caldera complex (Grocke et al., 2017a, 2017b) lying approximately 35 km north of La Pacana. A minimum DRE volume of 800 km^3 has been constrained for the Tara eruption (Grocke et al., 2017a), placing it intermediate between the Atana and Toconao eruptions and other ignimbrites in the APVC. Radiometric dating by the $^{40}Ar/^{39}Ar$ technique indicates eruption at 3.49±0.01 Ma (Salisbury et al., 2011), consistent with the youngest U-Pb zircon age (Kern et al., 2016). Quartz-hosted melt inclusion analysis has been used to constrain pre-eruptive water contents of up to 6.0 wt.% H_2O, in agreement with magma storage pressures of about 200 MPa and temperatures of 800-850°C, as derived from amphibole thermobarometry (Grocke et al., 2017a). $^{87}Sr/^{86}Sr$-isotope ratios of bulk-rock samples span the range 0.709380–0.713159, similar to the observed variability for the Atana and Toconao eruptions.

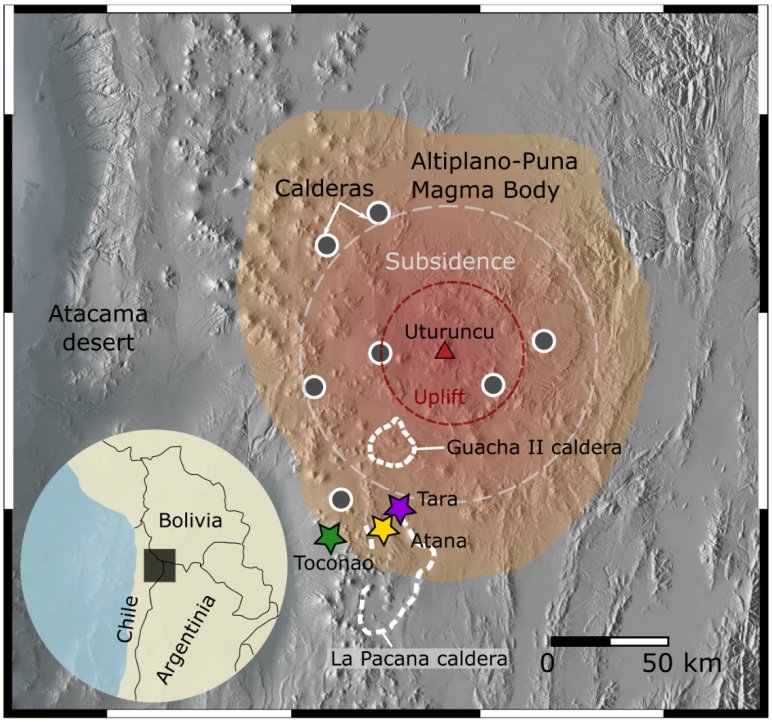

Figure 1. Sampling locations of the Atana (yellow star), Tara (purple star), and Toconao (green star) ignimbrites in the Altiplano-Puna Volcanic Complex. Outlines of the La Pacana and Guacha II calderas are indicated by white dashed

lines, while other calderas in the area are marked as grey dots. The extent of the mid-crustal Altiplano-Puna Magma body at 15 km depth (Ward et al., 2014) is projected on the relief map. Ground deformation pattern, centered at Uturuncu volcano in Bolivia (red triangle), are shown as red (uplift) and grey (subsidence) dashed lines (Pritchard et al., 2017). The inset shows the location of the study area in the border region between Chile, Argentina, and Bolivia. Relief Map was modified from MFF-maps under Creative Commons CC0.

3 Materials and Methods

2.1 Sample collection and processing

Samples of the Atana, Toconao, and Tara ignimbrites studied in this contribution were collected during a field campaign in Northern Chile in 2018. Photographic documentation of sampling locations can be found in supplementary Fig 1. The Atana ignimbrite sample was collected on the western flank of Cerro La Pacana, the resurgent dome of the caldera, at 4739±4 m altitude along a roadcut on Ruta 27 (GPS coordinates: 23°06'27.83" S, 067°29'42.13" W). The Tara ignimbrite was sampled inside the moat of the La Pacana caldera, where it occurs as isolated pillars and steep erosional cliffs (altitude: 4541±4 m; GPS coordinates: 23°03'19.13" S, 067°29'46.63" W). Sampling of the Toconao ignimbrite was carried out in its type locality at Quebrada de Jerez, 1 km east of Toconao village (altitude: 2531±4 m; GPS coordinates: 23°11'18.86" S, 067°59'31.11" W). The samples were processed to separate pumice-hosted plagioclases by crushing the rocks using a sledgehammer and hydraulic press at the University of Geneva, Switzerland. The crushed samples were washed in de-ionized water and dried in an oven at 40°C, before sieving to a size fraction >1 mm. Plagioclase crystals were then handpicked under a binocular microscope, mounted in epoxy resin, and polished in several steps under water and with diamond paste.

2.2 Electron-beam techniques

The epoxy mounts were coated with a 20 nm thick layer of carbon prior to imaging and analysis with electron beam techniques. Back-scattered electron (BSE) images of plagioclase zonation textures were acquired using a JEOL JXA 8200 Electron Probe Microanalyzer (EPMA) at 15 kV acceleration voltage and 15-20 nA beam current at the University of Geneva and at the Research Laboratory for Archaeology and History of Art, University of Oxford. Quantitative EPMA traverses were obtained using a JEOL JXA8530F Hyperprobe at the University of Bristol (UK) and at the Research Laboratory for Archaeology and History of Art (University of Oxford, UK) by wavelength-dispersive x-ray spectrometry (WDS). All measurements were obtained with an electron beam focused to ~2µm, beam current of 15-20 nA and acceleration voltage of 15 kV. The instruments were calibrated by repeated measurements of in-house standards, which were also analysed at the beginning, during and at the end of the plagioclase analyses. Measurements that showed totals outside the range 98.5 – 101.5 wt.% were discarded.

2.3 In-situ Sr isotope analysis

The *in-situ* Sr isotope analysis of plagioclase grains was conducted at the Bristol Isotope Group mass spectrometry laboratory in the University of Bristol. The Sr isotope analysis was carried out using Proteus, a unique collision cell, multi-collector inductively coupled plasma mass spectrometer with a pre collision cell, quadrupole mass filter (CC-MC-ICPMS/MS), coupled to a Teledyne^{TM} Photon Machines 193 nm Analyte G2^{TM} ArF excimer laser ablation system equipped with an aerosol rapid introduction system (ARIS) (Bevan et al., 2021).

The standard laser ablation conditions used for sampling were a laser fluence of 6 J cm^{-2}, a repetition rate of 10Hz, and laser pulse count of 600. The laser spot diameters varied between 50 and 85 µm. Laser ablation spot transects were positioned from plagioclase core to rim, perpendicular to zoning interfaces visible using back scatter electron (BSE) imaging. Each analysis was conducted using a fixed laser spot position. To exclude any periods of washout a single measurement cycle at the beginning and the end of ablation was rejected from the data.

During analysis the Proteus pre collision cell quadrupole was operated in band-pass mode, only permitting the stable ion transmission of 87 ± 5 u/e (unified atomic mass units per electronic charge) onward into the collision cell. Sulphur hexafluoride (SF_6) was utilised as the collision cell reaction gas to provide chemical resolution of Rb and Sr ions during analysis. This gas was demonstrated to display no observable reaction with Rb^+ and exhibits an efficient exothermic reaction with Sr^+ to form SrF^+ (Bevan *et al.*, 2021). The reaction gas mixture used was 5% SF_6 (99.99% purity) in He (99.9999% purity) which was further diluted using a separate He gas cylinder (99.999% purity). Total He and SF_6 collision cell gas flows used during analysis were 3 and 0.03 ml min^{-1}. The use of SF_6 as a reaction gas to provide Rb and Sr chemical resolution is so efficient that no ^{87}RbF correction is required in samples with Rb/Sr = 100 (Bevan et al., 2021). Thus, no ^{87}RbF correction was applied to the data presented here.

A 'low-resolution' aperture slit (DM/M~3000, 5-95% peak height definition) was used for all analysis, as this provides sufficient mass resolving power to avoid any measurement of cell-derived SF_3O^+ isobaric interferences. To enhance Sr ion sensitivity a cold plasma Ni skimmer cone was used (Bevan et al., 2021). Ion beam collection was achieved using an array of Faraday cup collectors, equipped with 10^{11} Ω feedback resistors, in a static measurement configuration. A total measurement integration time of ~ 60 seconds was used for all analyses. Measured $^{87}SrF^+$ /$^{86}SrF^+$ ratios were internally normalised to an ^{86}Sr /^{88}Sr ratio of 0.1194 using the exponential mass fractionation law (Russell et al., 1978) and the atomic Sr masses. The internally normalised $^{87}Sr/^{86}Sr$ ratios for the Atana plagioclase were externally normalised to internally-normalised measurements of in-house plagioclase standard Te-1, using a reference $^{87}Sr/^{86}Sr$ of 0.704000 determined by previous thermal ionisation mass-spectrometry measurements, to correct for any residual instrumental artefacts (Bevan et al., 2021). A more detailed description of the *in-situ* Sr isotope method used in this study is provided in Bevan et al., 2021.

2.4 Age correction of $^{87}Sr/^{86}Sr$

Continued beta decay of ^{87}Rb may have led to ingrowth of the stable ^{87}Sr in plagioclase crystals and groundmass glasses long after the cooling of the ignimbrites, given their eruption ages of several million years. To test the significance of this effect in plagioclase, a subset of crystals from each of the studied eruptions were analysed for $^{85}Rb/^{88}Sr$, which was externally normalised to NIST SRM 610 to calculate the sample $^{87}Rb/^{86}Sr$ ratio. Using the age equation of the form:

$$\left(\frac{^{87}\mathrm{Sr}}{^{86}\mathrm{Sr}}\right)_{\mathrm{initial}} = \left(\frac{^{87}\mathrm{Sr}}{^{86}\mathrm{Sr}}\right)_{\mathrm{observed}} - \frac{^{87}\mathrm{Rb}}{^{86}\mathrm{Sr}} e^{((\ \mathrm{t})-1)} \ ,$$

where is 1.3972 $\times 10^{-11}$ a^{-1}, the decay constant of ^{87}Rb (Villa et al., 2015), and t is the relevant eruption (Salisbury et al., 2011). The calculations indicate that radiogenic ingrowth in plagioclase crystals of the considered eruptions is smaller than the analytical uncertainty and is thus not considered further. All glass analyses presented in the manuscript have been corrected to initial values at the eruption age using the same approach.

2.5 Diffusion modelling

To constrain the maximum timescales of plagioclase crystal residence we model the diffusive equilibration of Sr-isotopes in plagioclase at pre-eruptive magmatic temperatures. Diffusion coefficients for Sr equilibration in plagioclase have been determined experimentally by Cherniak and Watson (1994) for elemental (chemical) diffusion and by Giletti and Casserly (1994) using an isotopic tracer approach. We consider the latter experiments more applicable to model $^{87}Sr/^{86}Sr$ diffusion in plagioclase, given the diffusion style, major element compositional and temperature range (An2-An96; 550-1300°C) of the experimental calibration. The Arrhenius equation for the tracer diffusion coefficient of Giletti and Casserly (1994) can be written as:

$$D = 2.92 \ \times 10^{-4.1X_{\mathrm{An}}-4.08} \ \exp\left(\frac{-276000}{\mathrm{RT}}\right),$$

where X_{An} is the molar fraction of anorthite in plagioclase, R is the ideal gas constant, and T is the temperature in Kelvin. To account for the spatial dependence of the diffusion coefficient along the X_{An} profile, we solve the one-dimensional diffusion equation of the form:

$$\frac{\partial C}{\partial t} \ = \ \frac{\partial}{\partial x}\left(D(x)\frac{\partial C}{\partial x}\right),$$

where C is $^{87}Sr/^{86}Sr$, t is time in seconds, and x the spatial coordinate in meters. We use an explicit finite difference method to solve the diffusion equation numerically (Costa et al., 2008; Dohmen et al., 2017; Weber et al., 2019). As D is variable as a function of space, which is constrained by the X_{An} profile, it must be evaluated between numerical nodes to maintain accuracy of the solution. The discretised diffusion equation takes the form:

$$\frac{\partial}{\partial x}\left(D(x)\frac{\partial C}{\partial x}\right) \mid_i = \ \frac{D_{i+\frac{1}{2}}\frac{C_{i+1}-C_i}{\mathrm{dx}} - \ D_{i-\frac{1}{2}}\frac{C_i-C_{i+1}}{\mathrm{dx}}}{\mathrm{dx}} \ ,$$

where i is the index of the numerical node, dx is the spatial dimension of a numerical grid point. The An and Sr-isotope profile for each modelled crystal were interpolated to 700 numerical grid points using a cubic spline fit. The left boundary of the Sr -isotope profile, corresponding to the outermost rim in contact with melt, was fixed at its initial value throughout the simulation, thereby treating the melt as an infinite reservoir able to diffusively equilibrate with the crystal. In cases of contrasting outermost rim and glass compositions, we additionally ran simulations in which the outer boundary was set at the observed glass Sr-isotope ratio. A zero flux boundary conditions was employed at the end of the right side of the profile in the interior of the crystal. Initial conditions in the diffusion modelling and used temperatures are discussed in the main text.

3 Results

3.1 Textural and geochemical characterization

A total number of 47 crystals for the three studied eruptions i.e. Atana: n=15, Toconao: n=19, and Tara: n=13, have been imaged using back-scatter electrons (BSE) to reveal their chemical zonation pattern. A representative selection of the zoning types of these crystals is shown in Fig. 2 and the full set of BSE images that were collected within the course of this study are available in the electronic supplementary materials. The imaged grains span a wide range of textural types, but are typically subhedral in shape with facetted rims and partially broken faces along cleavage plains that may either be attributed to crushing during sample preparation but may also reflect volcanic processes (van Zalinge et al., 2018). Although the zoning is complex with multiple resorption and overgrowth horizons, the pattern in most crystals can be described as normal zoning with higher An contents in the cores compared to overgrowth rims. Several common and distinct features are evident between samples from different eruptions. Atana plagioclase show the most severe zonation pattern with multiple dissolution horizons, patchy and sieve textures in crystal cores that are present in 13 out of 15 imaged grains. Later stages of crystal growth prior to Atana eruption have resulted in oscillatory or multi-step rim formation of typically a few 100 µm thickness and lower An contents. Boundaries between the described growth zones frequently show sudden shifts in BSE intensity, with or without the presence of resorption surfaces, indicating that the crystals have experienced drastic shifts in conditions during their growth history. Comparable zoning textures of relatively high An content in remnant crystal cores, however with less severe reaction textures, are observed in 10 out of 19 crystals from the Toconao eruption. Like Atana plagioclase, overgrowth rims in Toconao grains show weak oscillatory zoning that comprise the bulk of most grains. The described textures of Atana and Toconao plagioclase are similar to Tara grains, yet a distinct feature in the BSE images of the latter eruption is the presence of more pronounced resorption horizons in the interior of the crystals, resulting in greater amplitude of compositional oscillations. Such horizons are present in 5/13 grains at distances of 200 to 1000 µm from the crystal rim. Taken together,

the observed zonation pattern for the three eruptions are similar in that they record oscillatory overgrowth of compositionally distinct pre-existing grains but no evidence for large scale reheating of the system, which would be manifest in crystal rims as either pronounced resorption surfaces or reverse zonation with high BSE intensity.

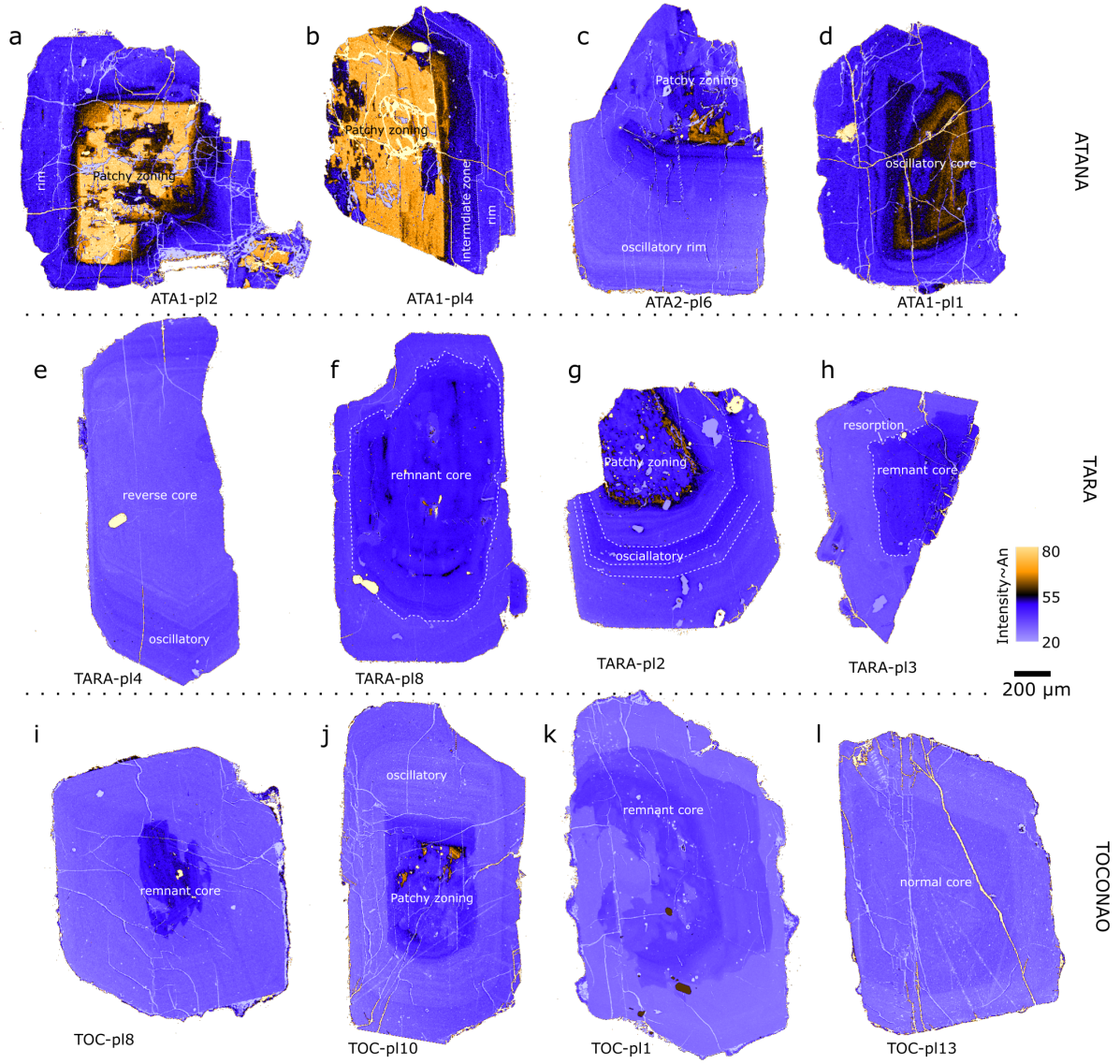

Figure 2. Back-scatter electron images of plagioclase crystals from the Atana (a-d), Tara (e-h), and Toconao (i-l) eruptions. Greyscale backscatter electron intensities were recolored to enhance the visibility of prominent zonation features

using the software package ImageJ. The color scale is proportional to the major element composition of the crystals, with blue color tones corresponding to lower An-contents and yellow colors indicative of higher An contents in plagioclase.

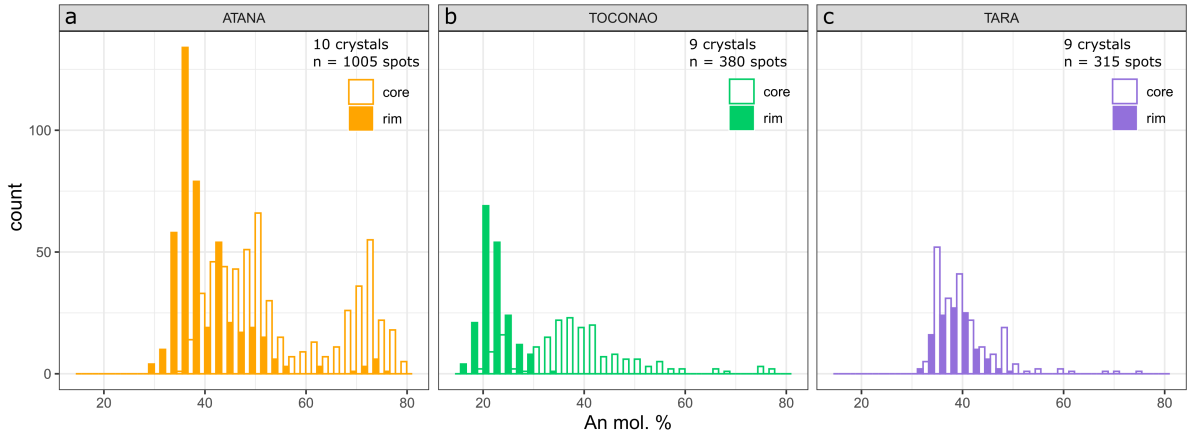

Figure 3. Histograms of molar anorthite contents of plagioclase crystals from the a) Atana (orange), b) Toconao (green), and c) Tara (purple) ignimbrite. In each case, filled columns represent crystal rim compositions and filled columns are plagioclase core compositions that have been assigned based zonation textures in BSE images. Atana and Toconao histograms show multi-modal distributions of rim and core compositions, while Tara samples are more restricted and uni-modal in plagioclase chemistry.

To quantify the compositional variation in major and minor elements of plagioclase, 28 crystals (10 Atana, 9 Tara, and 9 Toconao) were chosen for EPMA analysis. Our dataset comprises 1700 spot analysis (Atana: 1005, Tara: 315, Toconao: 380), with spacing of 15 to 40 µm between adjacent measurement spots for all grains, except for 8 Atana crystals that were measured with higher spatial resolution of 5-10 µm. Molar anorthite (An) contents span a wide range of An29-80 for Atana, An30-76 for Tara, and An15-77 for the Toconao eruption (Fig. 3a, b). These findings expand the ranges of previously published plagioclase data, namely An35-49 for Atana and An12-30 for Toconao (Lindsay et al., 2001b). Plagioclase compositions of the Tara ignimbrite are constrained to vary between An30-76 (Fig. 3c), expanding the previously reported range of An30-66 (Grocke et al. 2017a). Both minor reverse and normal zonation pattern are evident (Fig. 2), resulting in no systematic difference between crystal cores and rim compositions (Fig. 3). Core-rim differences are, however, pronounced in the Atana and Toconao samples. Compositional distributions of An (mol.%) contents for the Atana and Toconao eruptions are bimodal, with prominent peaks between An35-42 for Atana and An20-23 for Toconao that correspond texturally to crystal rim compositions. Core compositions for Atana crystals are multi-modal with peaks between An40-55 in oscillatory zoned grains, and An65-80 in crystals with sieve or patchy zoned cores. Toconao plagioclase cores span a

wide range (An20-80) but show a dominant peak between An30-50, overlapping with the mode of Atana rim and oscillatory core compositions. Considering the close temporal and spatial association of the Toconao and Atana eruptions, and that the crystal-poor Toconao rhyolite may represent an extracted liquid from the larger crystal-rich dacitic reservoir that fed the Atana eruption (Lindsay et al., 2001b), a petrogenetic link between the overlapping crystal populations could be expected. However, FeO_t contents of Atana plagioclase span a much narrower range of 0.23-0.25 wt.% (1^{st} to 2^{nd} quantile) at An30-50 compared to Toconao plagioclase (FeO_t = 0.15-0.23 wt.%; 1^{st} to 2^{nd} quantile), indicating that the two eruptions have separate and distinct petrogenetic histories (Fig. 4a).

The relation of major and minor element zonation in plagioclase can be further used to gain insights into pre-eruptive magmatic conditions during crystallization. The transition from crystal cores to rims of most of the analysed Atana, Toconao, and Tara plagioclases, show sudden drops in An content on the order of 10 - 40 mol.% (Fig. 4b; Fig. 5). These shifts in An may be associated with drops and increases on the order of 0.05 to 0.2 wt. % FeO, but in some cases FeO remains invariant with respect to An (Fig. 4b, Fig. 5). Petrological experiments show that the An content is positively correlated with temperature, pH_2O and more mafic melt chemistry (Cashman and Blundy, 2013), whereas FeO is mostly sensitive to fO_2 and the Fe content of the melt (Wilke and Behrens, 1999). Anorthite-dependent partitioning calculations (Bindeman et al., 1998) using a range of bulk-rock, melt inclusion and groundmass compositions for the three studied eruptions indicate a strong melt chemical control for grains showing large core to rim variation. These calculations do not account for the fO_2 dependence of Fe partitioning in plagioclase, but a comparison of predicted partition coefficients using the Bindeman et al., (1998) model and experiments of Wilke and Behrens (1999) show good agreement at fO_2 values relevant for the three eruptions considered here (Lindsay et al., 2001; Grocke et al., 2017; supplementary Fig. 3). High An cores (~An60-80) in Atana samples are consistent with crystallisation from liquids similar to the bulk-rock dacite and minor andesite inclusions (Fig. 6a), while more evolved Toconao (~An30-50) and Tara (~An30-50) cores reflect growth from mostly rhyolitic melts (Fig. 6b, c). While this is consistent with a strong melt chemical control on the observed compositional variation, the shift in An content without co-variation in FeO that is observed in several crystals of each eruption (Fig. 5b, d, e, f) is more consistent with a change in pre-eruptive pH_2O. Additionally, in some crystals FeO and An contents, show a linear increase towards the outermost rim (Figs 5a, b, d, e), which could be indicate progressive heating of a mush reservoir. We test the significance of this hypothesis by using two plagioclase-liquid models to translate increasing An contents into temperature changes (Putirka, 2005; Waters and Lange, 2015). Using a fixed melt H_2O content of either 4 or 7 wt.%, total pressure between 200 and 400 MPa, and the Atana groundmass glass composition (Lindsay et al., 2001b), the observed linear increase in An content of 10 mol.% can be translated into about 10 to 20°C. Based on water saturated experiments

for dacite bulk-rock compositions at 200 MPa at temperatures < 800°C (Caricchi and Blundy, 2015), temperature variation of 10-20°C could translate into a melt fraction change of about 10%, which is unlikely to have generated the eruptible magma in the case of the Atana eruption. In summary, the An-FeO systematics of plagioclase indicate a wide variety of different histories for individual crystals that experienced changes in melt chemistry and pH_2O during their growth.

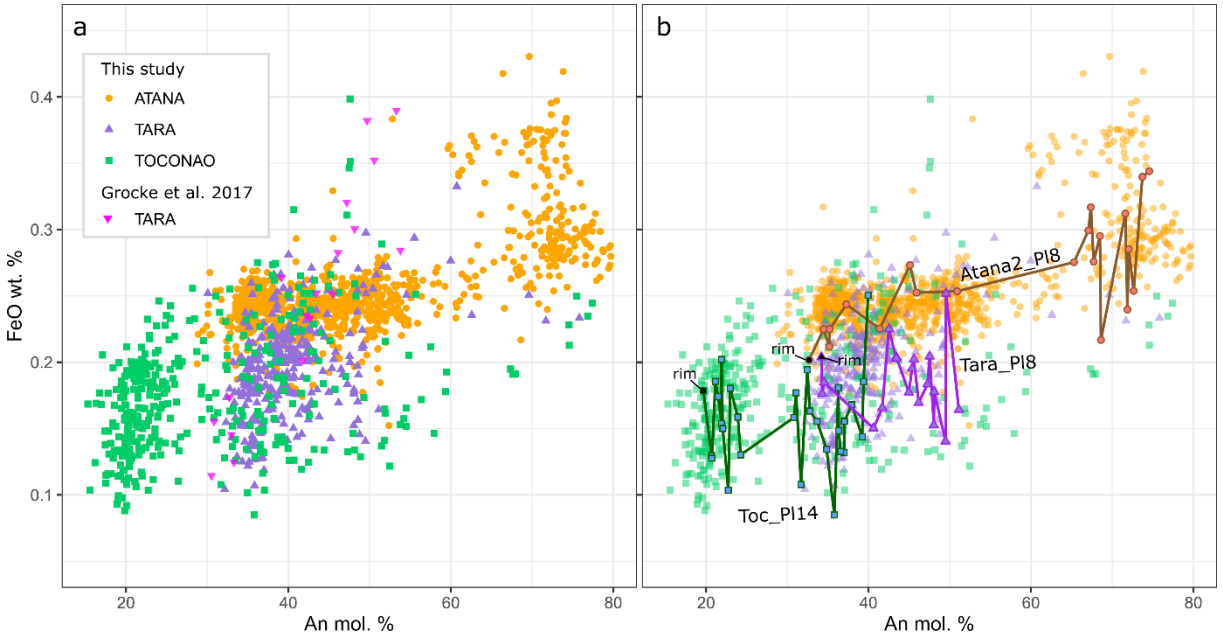

Figure 4. a) Anorthite (An - mol.%) versus total FeO (wt.%) in plagioclase from the three studied ignimbrites. Color coding and symbols reflect the eruption: Atana (orange dots), Tara (purple triangles), and Toconao (green squares). Data for the Tara eruption from Grocke et al., (2017) were filtered for analytical totals between 98.5 and 101.5 wt.% and are shown as pink triangles. Published plagioclase FeO contents for the Atana and Toconao eruptions (Lindsay et al., 2001b) are reported to one decimal place and are therefore not shown. b) Sample data as in a) but with plotted trajectory of a single crystals for each of the eruption with corresponding colors.

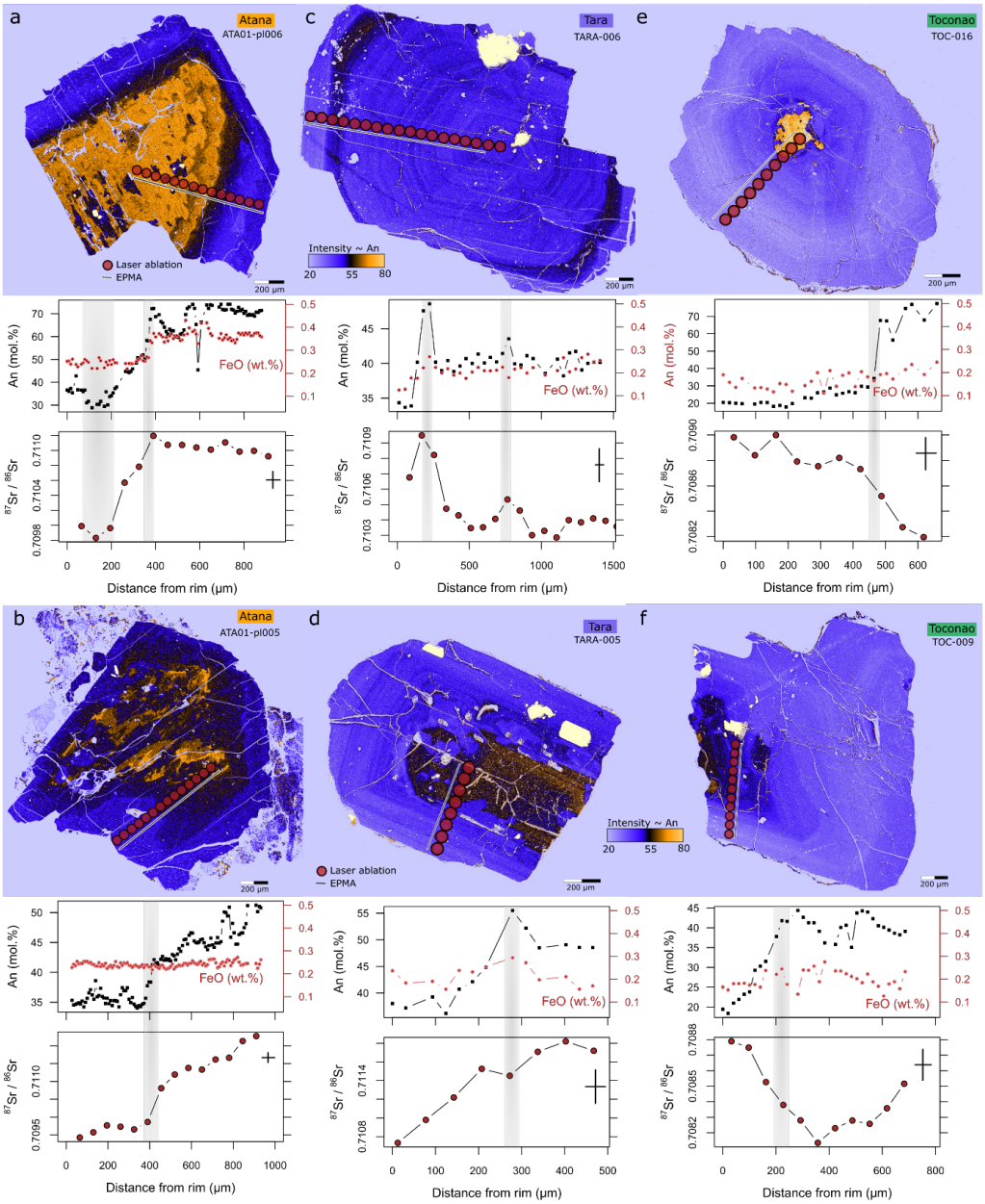

Figure 5. Profiles of analytical traverses (EPMA: black lines; LA-MC-ICP-MS: red spots) through selected plagioclase crystals are shown on BSE images. Greyscale intensity of the BSE images was color coded for An content. Major and minor elemental zonation traverses (An: black squares; FeO: red dots) and $^{87}Sr/^{86}Sr$ are shown for each crystal versus distance from the crystal rim

(µm). Black shaded areas indicate correspondence between EPMA and isotope traverses. (a-b) Atana crystals, (c-d) Plagiolcase from the Tara eruption, and (e-f) crystals from the Toconao ignimbrite. Representative error bars (2SE) and spatial resolution are shown for each isotope profile as black cross.

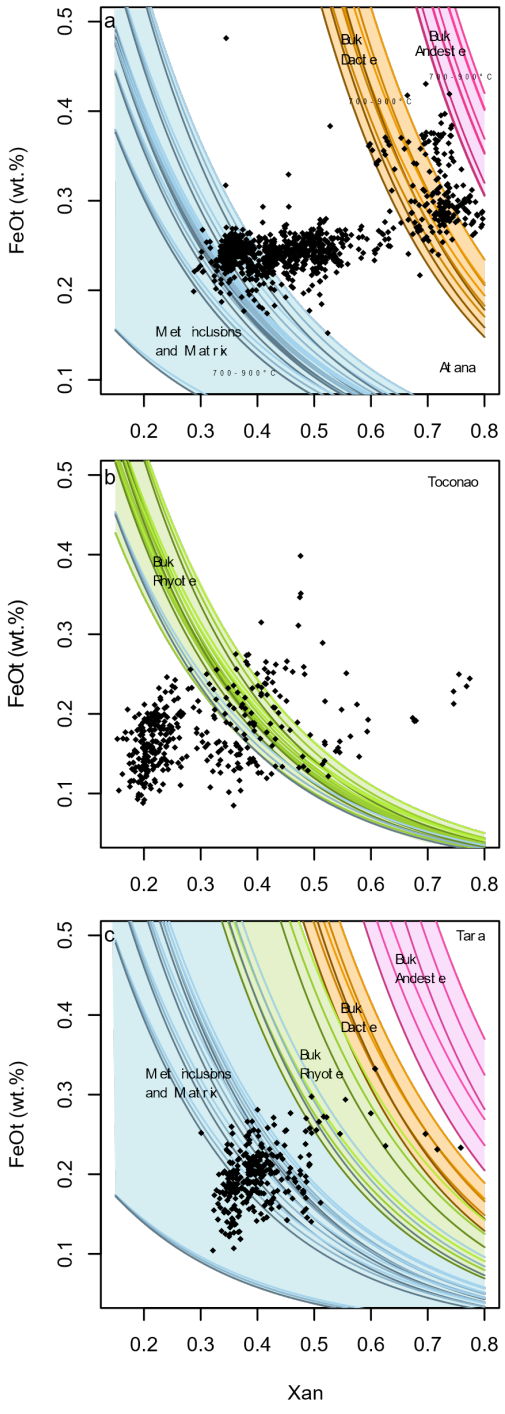
a
Buk
Dacite
Buk
Andesite
700-1000°C
700-900°C
Melt inclusions
and Matrix
700-900°C
Atana
b
Toconao
Buk
Rhyolite
c
Tara
Buk
Andesite
Buk
Dacite
Buk
Rhyolite
Melt inclusions
and Matrix
FeOt (wt.%)
Xan
0.1
0.2
0.3
0.4
0.5
0.6
0.7
0.8

Figure 6. Molar fraction of anorthite (Xan) versus FeOt (wt.%) for all plagioclase crystals from the three studied eruptions a) Atana, b) Toconao, and c) Tara. Colored lines in each plot show equilibrium partitioning of FeO in plagioclase for a range of bulk-rock and glass compositions for each of the eruptions (Lindsay et al., 2001b; Grocke et al., 2017b) in the temperature range 700 (colored darker lines) to 900°C (brighter lines) using the An-dependent partitioning relations of Bindeman et al., (1998). Melt inclusion and groundmass glasses are shown as blue, bulk-rhyolites as green, bulk-dacite as orange, and bulk-andesite as pink lines.

3.2 Crystal Sr-isotope stratigraphy

Plagioclase crystals from all three studied eruptions show considerable $^{87}Sr/^{86}Sr$ zonation pattern in core to rim traverses, reflecting changes in melt composition in the run-up to these events. The Sr isotopic composition in Atana crystals ranges from 0.7082 to 0.7123 (representative 2SE uncertainty: ±0.0002), which is larger than the spread of 0.7094 to 0.7116 recorded by published bulk rock compositions (Lindsay et al. 2001b), but similar to the total $^{87}Sr/^{86}Sr$ bulk-rock diversity of various APVC ignimbrites (Kay et al., 2010). Toconao plagioclases record Sr-isotopic compositions of 0.7080-0.7100, significantly lower compared to published values for bulk pumices of 0.7106-0.7131 (Lindsay et al. 2001b), while Tara crystals range from 0.7093-0.7118, overlapping but lower than published bulk-pumice analyses ($^{87}Sr/^{86}Sr$ = 0.7094-0.7132) for this eruption (Grocke et al. 2017b). These differences likely reflect the limited number of crystals analysed in this study, given the highly heterogeneous compositions of both crystals and bulk-rock analyses. As shown in Fig. 7, Sr-isotope profiles for each of the three eruptions show a common and systematic pattern of high isotopic diversity in crystal cores, evolving in strong gradients towards crystal rims that clearly show less isotopic variability compared to the interiors. Furthermore, the outermost rim composition records a common isotope ratio of 0.7094-0.7095 in 7 out of 10 crystals for the Atana eruption, 0.7088-0.7092 for Toconao (9/9 crystals), and 0.7105-0.7108 for Tara plagioclase (9/9 crystals). $^{87}Sr/^{86}Sr$ of outermost crystal rims for Atana and Toconao plagioclase coincides with the matrix glass composition of the ignimbrites, showing that the final stage of plagioclase growth reflects the carrier melt of the eruptible magma feeding each eruption. Tara glass compositions are on average lower compared to the outermost crystal rim compositions but mostly in agreement within measurement uncertainty. As the Sr isotope ratio in plagioclase records the melt isotopic composition at time of growth, which may later be modified by diffusive re-equilibration, this convergence of $^{87}Sr/^{86}Sr$ documents a drastic change in melt chemistry prior to each eruption. More importantly, the more homogeneous isotope ratio towards the rim of crystals suggests that the final eruptible magma that fed the three eruptions emerged by digestion of multiple distinct crystal populations, which must have separately developed in space and/or time, each of them undergoing their own distinctive evolution during growth from melt together with variable degrees of crustal contamination.

The processes that led to the amalgamation of the isotopically diverse crystal population prior to the Atana, Toconao and Tara eruptions can be further understood by tracing the evolution of $^{87}Sr/^{86}Sr$ and FeO in the melt. Using An-dependent partitioning relations (Bindeman et al., 1998), we invert plagioclase FeO contents into equivalent melt concentrations (Fig. 8) and link the melt evolution to textural features observed in BSE images (Fig. 5). High An crystal cores show melt equivalent FeO contents between 1.2 and 4.9 wt. %, consistent with their derivation from evolved andesitic or dacite melts and depletion of FeO contents during crystallization processes. The Sr-isotopic composition of high An cores vary between 0.7082 and 0.7111 with several trajectories of FeO depletion at different $^{87}Sr/^{86}Sr$, indicating that crystallization of individual magma aliquots that led to the formation of these cores occurred from a wide range of melts with variable degrees of crustal contamination. In contrast, rim compositions show melt equivalent FeO contents of mostly below 1 wt.%, implying that they grew from rhyolitic melt compositions. While FeO contents of the melts during crystallization of crystal mantles and, in particular, rims have been restricted, Sr-isotope compositions of plagioclase, which reflect the melt composition, show large variation. Such changes are inconsistent with simple crystallization or crustal assimilation scenarios but can be explained by progressive convergence of Sr isotopes in mixing/mingling processes of diverse crystal-rich magma pockets and/or disintegration of solid residue by an invasive rhyolite melt of different $^{87}Sr/^{86}Sr$ composition for the three cases. Our data do not permit to estimate mixing/mingling endmembers or proportions, but the incoming melt may have merged a larger number of isotopically distinct crystal populations, which permits the definition of simple binary endmembers using a steep mixing hyperbola (Fig. 8b). In summary, the isotopic and geochemical systematics of Atana, Toconao, and Tara plagioclase crystals record a late stage convergence related to mixing/mingling of a rhyolite melt and diverse crystal populations without evidence for large-scale heating. This hybridization process must therefore be related to an increase in melt fraction at relatively low pre-eruptive temperature.

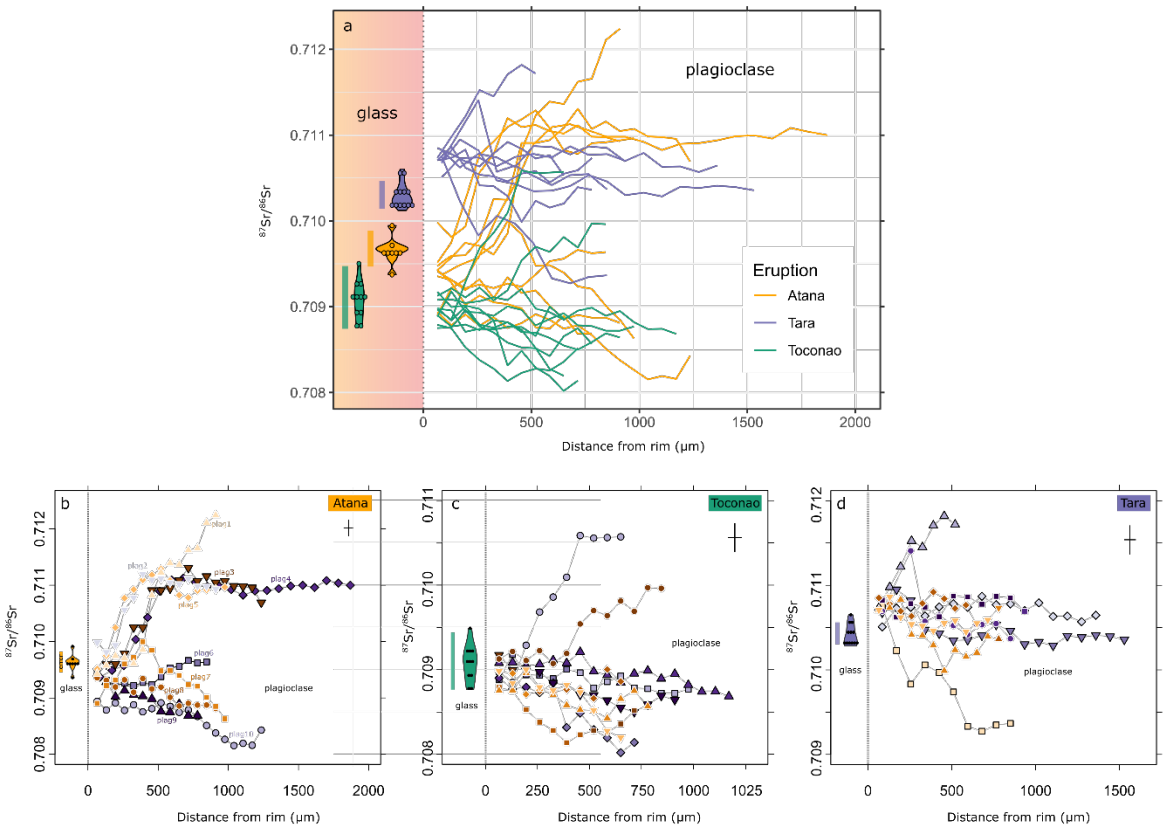

Figure 7. Sr isotopic traverses through plagioclase and groundmass glass compositions for the three studied eruptions (Atana: orange, Tara: purple, Toconao: green). a) $^{87}Sr/^{86}Sr$ analyses of glasses are shown as two-sided kernel density distributions (violine plots) in the shaded area. Vertical bars are representing analytical uncertainties for a single groundmass spot analysis (2 SE). The lines show analytical traverses as a function of distance from the crystal rim for all crystals, color coded for the different eruptions. b, c, and d) are close-up views for the Atana, Toconao and Tara eruptions, respectively. Symbols and colors reflect different crystals, spot size and analytical uncertainty are indicated as cross on the upper right side in each case. Representative 2SE uncertainties for the isotope measurements are ±0.0002.

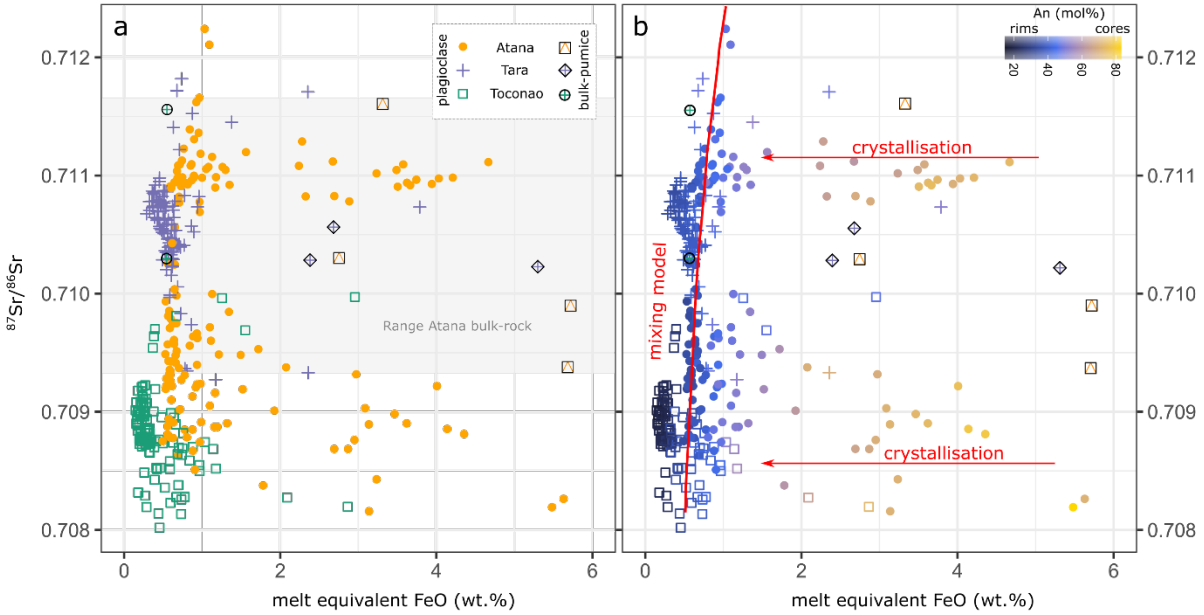

Figure 8. Melt equivalent FeO (wt.%) content versus $^{87}Sr/^{86}Sr$ of plagioclase. a) Orange colored dots represent Atana, purple crosses Tara and green squares Toconao samples. The range of bulk-rock compositions for the Atana eruption in shown as grey shaded area. b) Symbols are the same as in a) but color coding reflects the molar An content of plagioclase. The red arrows illustrate the trajectory during crystallization at a specific Sr isotope composition. The red line is a steep mixing hyperbola.

3.3 Timescales of eruptible magma residence

The strong Sr-isotope zonation gradients in plagioclase allows to reconstruct the maximum time that the crystals could have resided in the final assembled eruptible magma by means of diffusion chronometry. As described above, amalgamation of the eruptible magma is recorded by plagioclase crystals as a convergence process, creating a common isotopic composition in most crystal rims, while retaining much larger diversity in crystal cores. The isotopic disequilibrium between cores and rims, which must have been in local isotopic equilibrium with the carrier melt shortly prior to eruption, induces a chemical potential gradient that acted as a driving force for diffusive partial re-equilibration. This kinetic process is mostly dependent on the shape and magnitude of the gradient, and on temperature as an activation energy barrier must be overcome for the elements or isotopes to move to new sites in the crystal lattice. Pre-eruptive temperatures for the Atana ignimbrite have been estimated to vary between 750-790°C (Lindsay et al. 2001b) based on amphibole-plagioclase thermometry (Holland and Blundy, 1994), Fe-Ti oxide equilibration (Andersen et al., 1993), and two-feldspar thermometry (Ghiorso, 1984). Given that updated calibrations

of the Fe-Ti oxythermometer have been published, it is worth revisiting the pre-eruptive temperature estimates for the Atana ignimbrite. Using the touching titanomagnetite-ilmenite pair compositions presented in Lindsay et al. (2001b) in conjunction with the oxide geothermometer of (Ghiorso and Evans, 2008) yields median temperatures of 754°C, lower compared to previous estimates, but in very good agreement with estimates from amphibole-plagioclase temperatures (Holland and Blundy, 1994; supplementary Fig. 3). Given the match of different independent thermometers and accounting for the uncertainty of the estimates, we use a temperature of 754°C±30°C in subsequent diffusion calculations for the Atana ignimbrite. Temperature estimates for the Toconao eruption based on the two-feldspar thermometry are more limited but also indicate a temperature of 754°C, which given the uncertainty of the method (±30°C) agrees well with previous estimates (730-750°C; Lindsay et al. 2001b). We therefore explore the same range of temperatures as for Atana (i.e. 724, 754, and 784°C) in diffusion calculations for Toconao. Pre-eruptive temperatures of the Tara magma have recently been constrained based on amphibole-plagioclase pairs (Holland and Blundy, 1994) and touching Fe-Ti oxides (Ghiroso and Evans, 2008) and are in good agreement with each other (Grocke et al., 2017b). Tara diffusion calculations were carried out using the median temperature of these estimates of 852°C and uncertainty of ±30°C.

Before diffusion timescales can be reconstructed from the zonation profiles, initial conditions need to be evaluated, which is best achieved by comparing the systematics of elements with contrasting diffusive mobilities. Interdiffusion of CaAl–NaSi in plagioclase has been shown experimentally to be sluggish even at much higher magmatic temperatures (Liu and Yund, 1992) than those considered here. Strontium isotopic tracer diffusion in plagioclase is, based on experiments (Giletti and Casserly, 1994), several orders of magnitude faster than CaAl–NaSi exchange, which implies that while An gradients remain stationary during protracted magma storage, Sr isotope profiles should undergo diffusive re-equilibration. Comparing the zoning pattern of An and $^{87}Sr/^{86}Sr$, we note that even though the resolution of EPMA (~2 µm) and Proteus spots (~80µm) is very different, the profiles show a strong resemblance, typified by corresponding major gradients (Fig. 5) and in some cases even minor features (Fig. 5a, b). A decoupled evolution of An content and Sr isotopes is observed in several grains, which may reflect a different history compared to the other crystals without the development of strong isotopic gradients or partial diffusive equilibration. The latter is, however, difficult to reconcile with the observed profile shapes, if the original isotopic profile shape showed similar coupling of An and $^{87}Sr/^{86}Sr$ as measured in the other crystals. Taken together, gradients and profile shapes indicate that the initial isotopic zoning pattern have not been drastically modified by diffusion but are mostly original crystal growth features, reflecting the isotopic composition of the melt. Any diffusion would only serve to smooth out the observed isotopic profiles.

The observation that Sr isotope profiles mostly reflect growth zoning rather than diffusive equilibration can be used to evaluate scenarios of eruptible magma

residence, as diffusion at pre-eruptive temperatures would have flattened and smoothed the observed gradients. As we cannot rule out that pre-eruptive diffusion has occurred, we focus here on 3 scenarios, assuming that the magma equilibrated with a melt composition similar to the common rim observed in each case for the great majority of crystals (Fig. 7). The first scenario (Scenario 0; Fig. 9a) represents a case in which the observed profile is considered to represent only growth zoning, in which case we can track the maximum time that the profile could have survived equilibration with the common rim composition before it diffuses out of the error margins given by the analytical uncertainty. We refer to these as 'survival timescales'. Survival timescales calculated using this approach for the Atana eruption (n=7; Fig. 10) span a wide range from 82 years to 23.8 ka, with most crystals recording maximum survival times <1000 years (median: 513 years). Modelled Tara crystals (n=6) yield the shortest maximum residence times ranging from 24 to 1986 years with a median of 137 years; Toconao plagioclase (n=4) could have resided in the eruptible magma for 977 years on average (range 301-5815 years). These estimates include crystals that do not show large gradients in $^{87}Sr/^{86}Sr$ yielding maximal timescales of several millennia. Most profiles for the Atana and Tara eruptions show survival timescales on the order of several decades to centuries, suggesting that the assembled eruptible magma has not existed in the crust for protracted periods of time (i.e. hundreds of thousands of years).

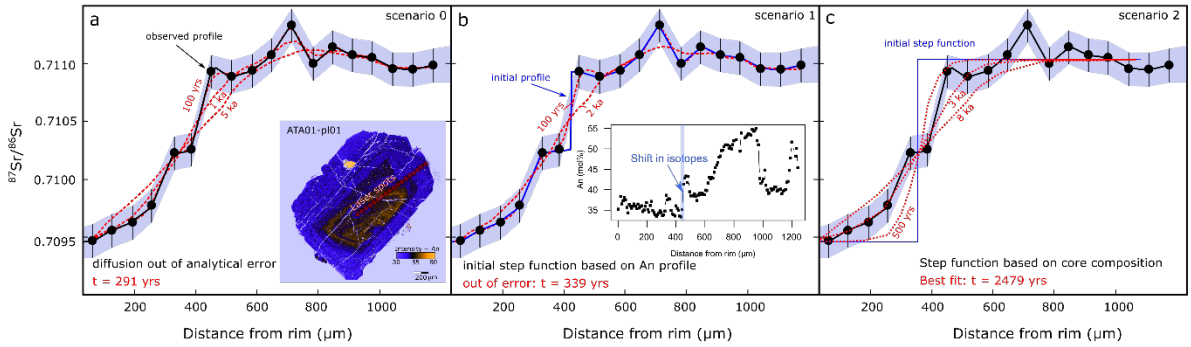

Figure 9. Illustration of different approaches to diffusion chronometry based on Atana crystal (ATA01-pl1). a) In scenario 0, the observed $^{87}Sr/^{86}Sr$ isotope profile is taken to be the initial profile and the time is tracked for diffusion out of analytical uncertainty. Red dashed curves show alteration of the observed (initial) profile after a 100 yrs, 1 ka and 5 ka of diffusive equilibration. b) Scenario 1: Based on a shift in An content (shown in the inset), the initial profile (blue line) is considered to be a step function. Red dashed curves illustrate the diffusive equilibration of the profile after 100 and 2000 years. c) Scenario 2 represents a case where the initial profile (blue curve) is assumed to be a step function over the entire observed gradient. Results of diffusion modelling after 0.5, 3 and 8 ka are shown as red dashed curves.

$^{87}Sr/^{86}Sr$ profiles may have been initially steeper than the observed profile and then relaxed diffusively to their observed gradients. We refer to these as 'relaxation timescales'. To estimate the impact of different initial conditions on the calculated maximum residence timescale, we carried out diffusion calculations in two additional scenarios (Fig. 9b, c). In Scenario 1, the initial profile shape is based on that of the An profile in cases where the gradient in Sr-isotopes is correlated with a sharp drop in An content (Fig. 9b), indicating that both features can be ascribed to a common process, but not observed in the Sr-isotope profile due to lower spatial resolution and precision of the laser spot analyses (Davidson et al., 2001). This criterion is only met for three crystals from the Atana eruption, yielding timescales which are ~50 to 100 years longer than the corresponding survival timescales. Additionally, where possible, a best-fit time was calculated for the observed profile of one crystal (Atana plag3_CR; Fig. 10), indicating a maximum residence timescale of 156 years at 754°C. Alternatively (Scenario 2), the initial Sr isotope profile may have taken the form of a step function across the entire length of the observed gradient (Fig. 9c), which results in timescales of 321 to 6556 years before diffusion would adjust the pattern to a shape like the observed profile within the analytical precision and spatial resolution of our measurements. However, we note that there is 1) no indication based on the An profile that such initial conditions are realistic and 2) that it is difficult to fit the observed profile from an initial step function spanning the entire gradient. We therefore suggest that calculation results of Scenarios 0 and 1, rather than Scenario 2, are more robust estimates of the maximum time that the crystals could have spent in the pre-eruptive magma.

While the convergence of $^{87}Sr/^{86}Sr$ isotopic compositions towards a common outermost rim of 0.7095 is recorded in most crystals of the Atana eruption, some feldspars show different rim compositions (Fig. 7a). This heterogeneity may be attributed to various effects, including the size of laser spots compared to outermost rim of crystals, heterogeneous isotope composition of the melt and/or entrainment of the crystals shortly prior to eruption with insufficient time for re-equilibration. Although, Sr-isotope heterogeneity may to some extent be possible within the error margins of our glass analyses, and natural variability has been documented for other dacitic large volume eruptions (Fish Canyon Tuff; (Charlier et al., 2007), the variability in glass compositions is too small to explain these differences. In either case, Sr diffusion in melts is several orders of magnitude faster than in plagioclase feldspar (Perez and Dunn, 1996), which implies that differences in melt composition can only be preserved, if they are created very shortly prior to eruption or if the eruptible magma assembly process and eruption initiation are contemporaneous. Our modelling indicates that entrainment of crystals with rim composition of 0.7086 could retain its chemical zoning for no more than 492 years at 754°C (197 years at 784°C; 1301 years at 724°C) emersed in a melt in equilibrium with the common rim composition of 0.7095 for the Atana eruption.

In summary, survival, and relaxation timescales of Sr isotope gradients in Atana and Tara plagioclase indicate that most crystals could not have spent more than

several decades to centuries in the assembled eruptible magma even when considering a conservative error margin of ±30°C on the pre-eruptive temperature estimate. Toconao plagioclase indicate longer maximum residence timescales on the order millennia. Although these timescales provide valuable insights into the upper time limit over which the eruptible magma existed in the crust prior to eruption, they also require that the growth and destabilisation process resulting in the accumulation and evacuation of eruptible magma must operate on even shorter timescales.

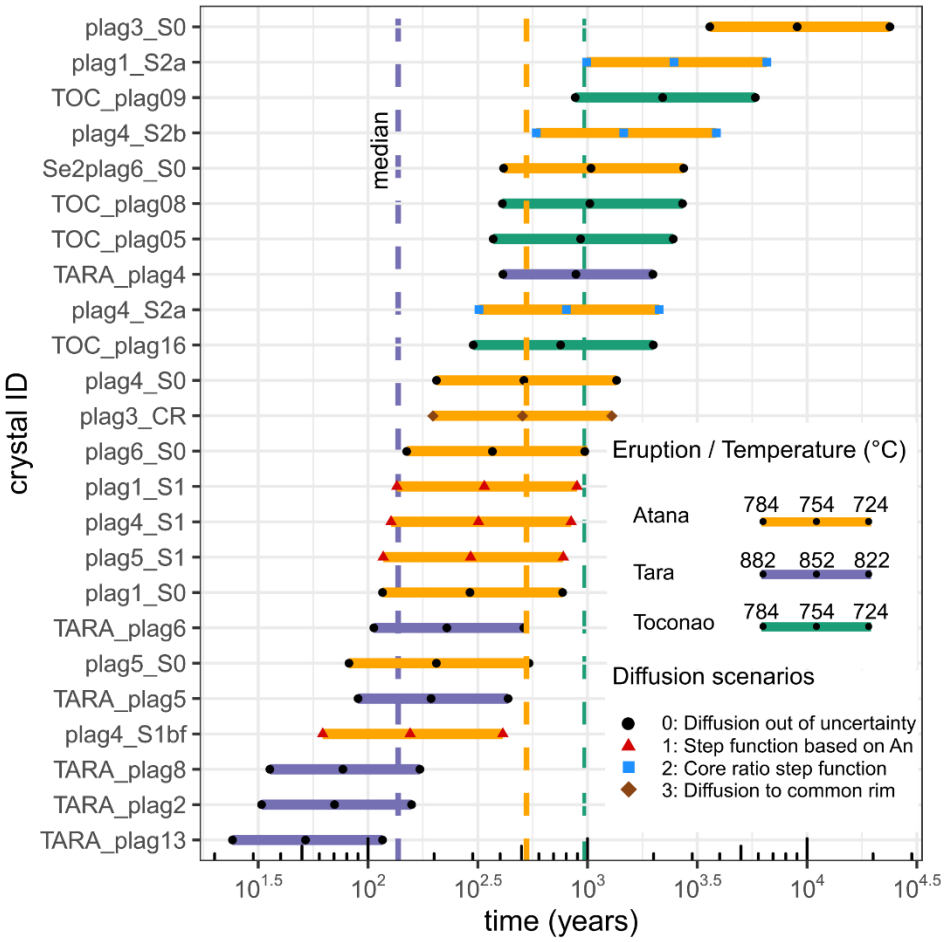

Figure 10. Summary of calculated diffusion timescales. Results are shown as log-scale ranked order plots of time in years for different crystals, with colors corresponding to the eruption: Atana (orange), Tara (purple), and Toconao (green). Three timescales are shown for each crystal reflecting the range of investigated temperatures. Symbols indicate the diffusion scenario, with black dots corresponding to scenario 0 (diffusion out of analytical error), red triangles

to scenario 1 (step function based on An content), blue squares to scenario 2 (Core ratio step function), and brown diamonds to scenario 3 (diffusion to common rim). Dashed lines are medians of all diffusion estimates for the three eruptions.

4 Discussion

4.1 Growth and destabilization of rhyolitic melt lenses

Field and petrological studies have shown that silicic large magnitude eruptions constitute a dichotomy in physico-chemical conditions of magma bodies, exemplified by crystal-poor rhyolites (e.g. Toconao ignimbrite) and crystal-rich dacites (or monotonous intermediates; e. g. Atana ignimbrite). Over the last decades, broad consensus has emerged in the interpretation that monotonous intermediate magmas represent erupted crystal mushes that have experienced an increase in melt fraction prior to eruption and that crystal-poor rhyolites originate through extraction of interstitial melt and gas from larger mush-dominated reservoirs that embody the source of monotonous intermediates (Bachmann and Bergantz, 2004; Cashman et al., 2017; Bachmann and Huber, 2019; Edmonds et al., 2019; Sparks et al., 2019). Various melt segregation mechanisms for the origin of rhyolitic melt lenses have been proposed, such as gas-driven filter pressing (Sisson and Bacon, 1999; Bachmann and Bergantz, 2006; Pistone et al., 2017), percolative reactive flow (Solano et al., 2012, 2014; Jackson et al., 2018), hindered settling or compaction-driven melt extraction (McKenzie, 1985; Bachmann and Bergantz, 2004; Lee et al., 2015; Hartung et al., 2019), operating over a wide variety of timescales ranging from days to hundreds of thousands of years (Edmonds et al., 2019). Our Sr-isotope diffusion results for the Toconao eruption, an exemplar of crystal-poor rhyolite, constrains the maximum timescale for the accumulation and destabilisation of the melt lens prior to this eruption to be on the order several centuries to millennia. This requires relatively fast melt extraction and accumulation, consistent with models of porous reactive flow in crystal mushes (Jackson et al., 2018), but requiring relatively large crystal sizes and water-rich magma in compaction-driven and hindered settling extraction scenarios (Hartung et al., 2019). Moreover, our finding of an isotopically distinct melt composition, and more variable FeO contents in plagioclase for the Toconao eruption suggest that this rhyolite does not simply represent an extracted differentiated liquid from the mush that gave rise to the subsequent Atana eruption (Lindsay et al., 2001b), but has undergone a separate prior evolutionary process. The observation that both crystal-poor rhyolites (i. e. Toconao) and crystal-rich dacites (i. e. Atana and Tara) record similar pattern of diverse pre-existing mush amalgamation by an invasive melt, suggests that both eruption types are associated with destabilisation of melt-rich magma lenses.

Hydrous rhyolitic magma lenses have densities that are invariably lower than those of their host crystalline mushes, favouring the development of gravitational instabilities that may lead to magma transfer and eruption at the surface. Assessing the timescale over which melt lens instabilities develop in crystal mushes

and comparing these estimates to our diffusion-derived maximum crystal residence times provides an opportunity to constrain the stability window for the presence of eruptible magma prior to large magnitude eruptions. Using analogue experiments Seropian et al., (2018) derived a formalism to calculate the timescales for the development of Rayleigh Taylor instabilities (RTI) in a case where the wavelength of the instability is larger than the width of the intrusion (confined case). The characteristic RTI time, over which the amplitude increases by a factor of ~2.72, is given by

$$t_{RTI,\ \ conf} = \frac{6\ \pi\ \mu}{\rho\ g\ L},$$

where μ is the viscosity of crystal mush in Pa s, Δ is the difference of crystal mush and melt lens density (kg m^{-3}), g is the acceleration of gravity in m s^{-2}, and L is the diameter of the melt layer in m. Timescales for cases in which the instability wavelength is smaller than the width of the melt length (unconfined case) can be calculated based on earlier work (Whitehead Jr and Luther, 1975) by:

$$t_{RTI,unconf.} = \frac{}{0.232\ g\ \ \rho\ h}\ \varepsilon^{-\frac{1}{3}},$$

where h is the thickness of the melt lens in meters and is the ratio of mush and melt lens viscosities in Pa s. In a first step, to constrain the impact of modelling variables, we explored a range of relevant variables for rhyolitic melt lenses using a Monte Carlo approach, calculating 10.000 random combinations of mush viscosities (10^{14}-10^{19} Pa s), mush and melt densities (2600-3000 kg m^{-3}; 2000-2500 kg m^{-3}), and melt lens diameters (5 – 80 km) for the confined case (Fig. 11a), and melt lens thickness between 50 and 500 m in the unconfined case (Fig. 11b). Confined instability timescales vary over a vast range of timescales spanning years at low mush viscosities to several hundred thousand years, while calculated instability timescales for the unconfined case are as short as 7 hours ranging to 62 days for the parameter space under consideration.

To better constrain instability timescales relevant in the more specific cases of the Atana and Tara eruptions, we calculated the melt density for these events using average groundmass glass analyses (Lindsay et al., 2001b; Grocke et al., 2017b) and partial molar volumes of the chemical components. The density calculations were performed using 3 kbar pressure, 4-5 wt.% H_2O, and temperatures of 754°C and 852°C for Atana and Tara, respectively. Geophysical estimates of mush viscosities for the Altiplano Puna Magma Body have been constrained to be on the order of 10^{16} to 10^{17} Pa s (Gottsmann et al., 2017). Although the diameter and thickness of the melt layer that accumulated in the mush prior to the eruptions are unknown, the diameter of the source calderas and eruptive volumes may be used as a proxy to constrain these variables. If the collapse caldera diameter 60x35 km for Atana and 20x30 km for Tara to some degree reflects the size of the accumulating melt lens and considering the DRE erupted melt volume for both eruptions, cylindrical (Volume = r^2 h, where r and h are the radius and height) and ellipsoidal melt lenses (Volume = 4/3 a b c, where a, b, c are the semi-axes) would require a thickness of 130 to 170

m for Atana and 220 to 300 m for Tara. Caldera dimensions for the Toconao eruption are unknown due to superposition with the younger and much larger La Pacana caldera but based on an erupted DRE volume of 1600 km^3, the collapse structure can be expected to be smaller than the Guacha II caldera, which would result in longer instability timescales (Fig. 11). Our calculations indicate that instability timescales in the confined case are on the order of 50-500 years for Tara and 30-300 years for Atana. Unconfined instability timescales for both eruptions are significantly shorter on the order of days to a few years. Both cases are consistent with a time window for the presence of eruptible magma in crystal mushes shorter than the maximum crystal residence time (decades to centuries) based on Sr isotope diffusion, in keeping with the emerging view that eruptible magmas are ephemeral in nature and develop over timescales relevant for volcano monitoring (van Zalinge et al., 2022).

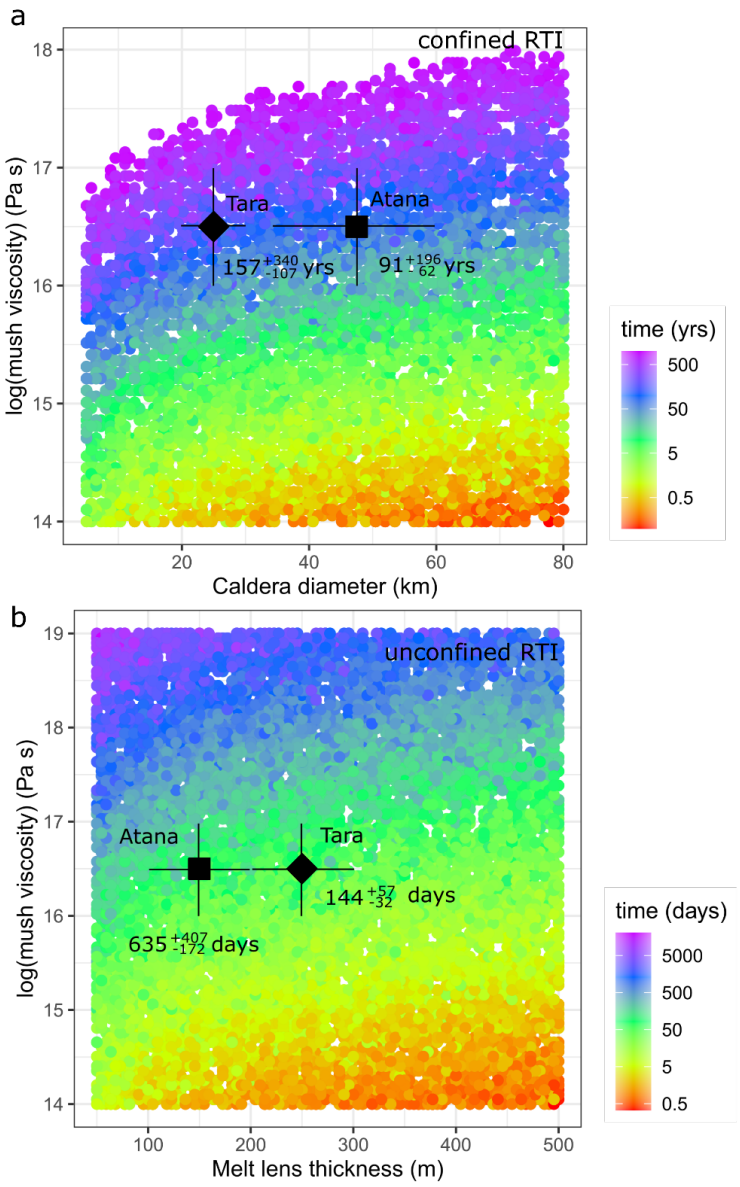

Figure 11. Gravitational instability timescales of melt lenses in crystal mush. Results are shown for the Atana (black square) and Tara (black diamond) eruptions and of monte carlo simulations color coded for time. Parameters used in the modelling are discussed in the main text. a) Log mush viscosity versus caldera diameter (i. e. approximately diameter of the melt lens) for confined Rayleigh Taylor Instabilities where the wavelength is larger than the diameter

of the melt lens (Seropian et al., 2018). For the sake of clarity only timescales < 1000 years are shown. b) Log Mush viscosity versus melt lens thickness (calculated from erupted volume and caldera diameter for Atana and Tara). Timescales (days) are for an unconfined case, where the wavelength of the gravitational instability is smaller than the length of the melt lens.

4.2 Detectability of precursors to supereruptions

Given the lack of observational experience with past large-volume eruptions, it remains unclear if we are currently capable of detecting the evolution towards a pending supereruption by geophysical volcano monitoring techniques. Although large-scale geophysical unrest has been observed prior to comparatively small explosive eruptions like Pinatubo in 1991 (McNutt, 1996), suggesting that similar features may be extrapolated to larger eruptions, the magnitude, timeframe and type of signals that may be observed remains obscure. Our petrological finding of a common pattern in melt-mush amalgamation in the run-up of three large magnitude eruptions can be tested against the resolution of different geophysical monitoring techniques. Tomographic imaging by seismic and magnetotelluric methods has revealed that many large caldera complexes are underlain by massive mush accumulations but mostly comprised of mush at low melt fraction within the resolution of these methods (e.g. Toba: (Jaxybulatov et al., 2014; Koulakov et al., 2016); Yellowstone: (Farrell et al., 2014; Huang et al., 2015); Altiplano-Puna-Complex: (Pritchard et al., 2018)). As discussed above, considering the dimensions of the source calderas for the Atana and Tara eruptions, melt and eruptible magma lenses of not more than a few hundred meters thickness can be expected, which even under favourable seismic or magnetotelluric network configurations will not be detectable by the resolution of these methods (Lowenstern et al., 2017). Alternatively, the assembly of melt lenses and/or amalgamation of eruptible magma may create ground deformation pattern, which are now routinely measured in volcanic settings by GPS or satellite-based interferometry (Poland and Zebker, 2022). The detectability of such a signal in association with the accumulation of melt lenses and disruption of pre-existing mush pockets depends on various factors, including the magnitude of thermally controlled viscoelastic effects, which should be prevalent in crystal mushes, and potential exchange flow of upwards percolating and melt and displacement of crystalline materials downwards. While much work has been focused on quantifying thermo-mechanical controls on surface deformation patterns (Del Negro et al., 2009; Hickey et al., 2016; Head et al., 2019; Morales Rivera et al., 2019), and integration of petrological models with surface geodetic studies (Weber and Castro, 2017; Trasatti et al., 2019; Townsend, 2022), deformation sources are typically modelled as an overpressure boundary condition on a cavity representing a magma body. New coupled models of melt flow in crystal mushes and ground deformation are required to test if destabilisation of melt lenses could create large scale uplift and subsidence pattern such as those observed in the Altiplano Puna Volcanic Complex.

The accumulation of a melt lens followed by invasive disruption of crystal mush

could lead to a measurable change in the gravitational field, given that mushes and rhyolite melts have different densities. To quantify the magnitude of such an effect, we modelled the change in the gravitational acceleration (g), caused by a cylindrical, low-density melt layer in higher density crystal mush (Telford et al., 1990):

$$g = 2\ \pi\ G \quad \{L + (z^2 + \ R^2\ )^{\frac{1}{2}} - [(z+L)^2\ + R^2]^{\frac{1}{2}}\},$$

where G is the gravitational constant (6.67*10^{-11} m^3 kg^{-1} s^{-2}), Δ is the density contrast of melt and mush (-300 to -500 kg m^{-3}), L is the thickness of the melt layer (100 – 300 m), R is the diameter (20 to 50 km), and z is the depth of the cylinder top below the surface (10 km if not stated otherwise). Depth estimates for the Atana and Tara magmas are prone to high uncertainties, but are of secondary importance in the gravity calculations (Supplementary Fig. 4). We used 10.000 random combinations of the parameters given above to quantify the gravity effect of melt lens accumulation over a timeframe of 20 to 2000 years (Fig. 12). Depending on the thickness of the lens, accumulation in less than 100 years results in strong gravity effects on the order of -0.20 to -0.02 mGal/year. Long-term growth over centennial and millennial timescales results in lower gravity effects, but ~90% of the calculations yield gravity signals that are within the current precision limit of modern gravimeters (up to -0.001 mGal; (Greco et al., 2020)). We suggest that high-precision gravity monitoring may provide crucial insights to evaluate if one or more of Earth's large caldera complexes are currently in the process of accumulating eruptible magma.

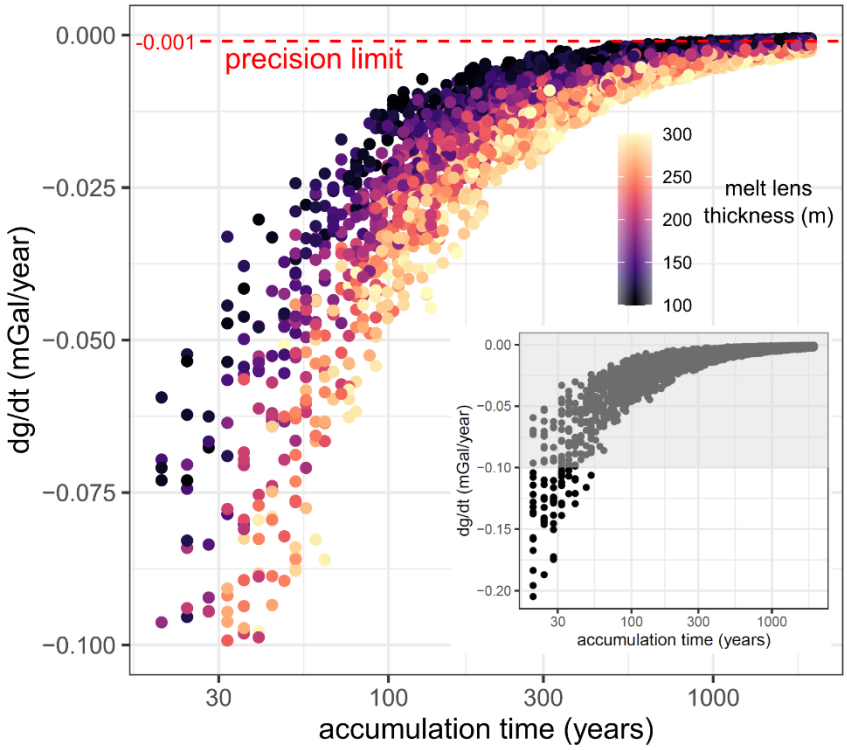

Figure 12. Gravity effect of an accumulating melt lens in crystal mush. Monte carlo results are shown for the rate of change in gravitational acceleration (dg/dt) in mGal/year versus the accumulation time of melt lenses. Color coding reflects the thickness of the accumulated lens. The limit of precision for state-of-the-art gravimeters of -0.001 mGal is indicated as a red dashed line. The inset shows the full range of dg/dt calculated over the parameter space considered. Only the grey shaded area is shown to aid comparison with the precision of gravimeters.

5 Conclusions

A conceptual summary of this study is provided in Fig. 13. Based on our petrological analysis and geophysical model calculations, we draw the following conclusions:

1. Sr-isotopes in plagioclase crystals from three Central Andean large magnitude eruptions (Atana, Tara, and Toconao) reveal a recurrent pattern of large isotopic diversity in cores that converge in steep gradients towards common values in crystal rims. This suggests that previously intruded, isotopically distinct mush batches with spatially and/or temporally distinct histories have been homogenized and mobilised by an invasive rhyolite melt before each eruption.

2. Isotopic compositions of glasses and plagioclase, as well as the plagioclase

An-FeO systematics show that the Toconao ignimbrite does not simply represent an extracted liquid from the mush that produced the Atana eruption. Both eruptions have tapped distinct environments of the batholitic reservoir.

3. Most plagioclase crystals cannot have spent more time in the eruptible magma than decades to centuries for the Atana and Tara ignimbrites, and centuries to several millennia for the Toconao eruption. These maximum crystal residence timescales provide an upper limit for the observation window for eruptible magma in these systems. Destabilisation of rhyolite melt lenses in crystal mush can proceed on timescales of years to centuries, typically shorter than the diffusion estimates, suggesting that eruptible magma pockets are ephemeral.

4. Calculations based on caldera dimensions, DRE erupted volumes, and indicate that in the case of the Atana and Tara eruption, the size of melt lenses and eruptible magma pockets was likely below the resolution of seismic and imaging techniques currently employed. The gravity effect of eruptible magma accumulation may, however, be resolved using state-of-the-art instrumentation under favourable conditions.

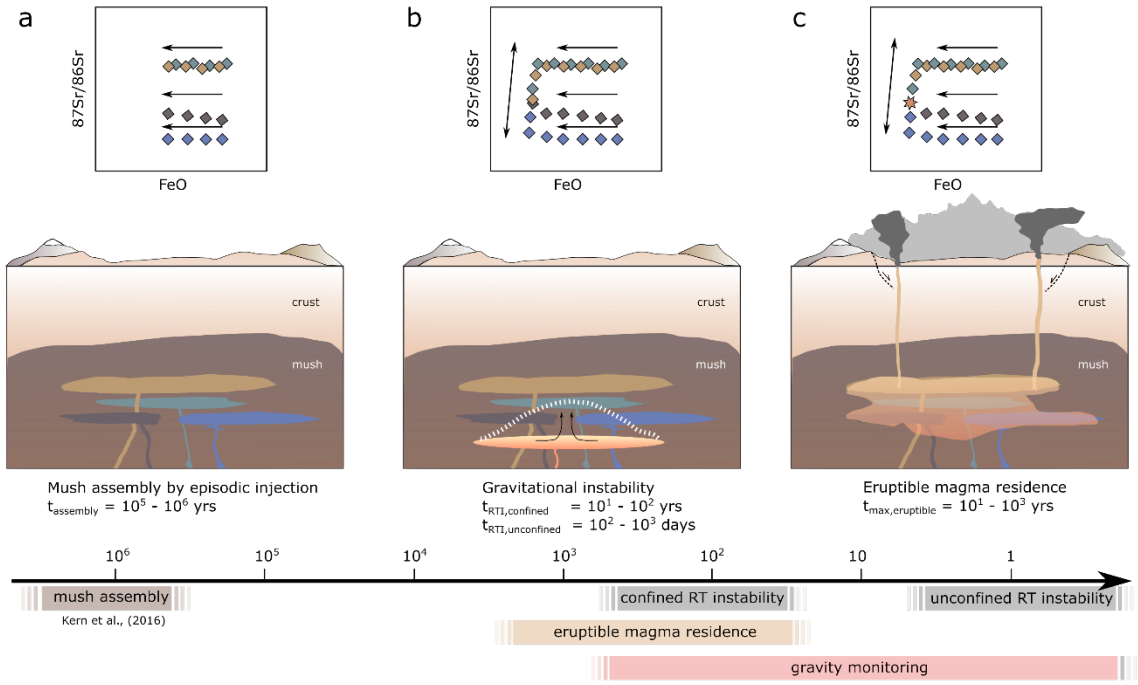

Figure 13. Conceptual summary of processes and timescales. a) Long-term mush accumulation on timescales of 10^5-10^6 years as indicated by zircon

geochronology (Kern et al., 2016). Pulsed injection of magma batches leads spatial and temporal heterogeneity that is reflected in different isotopic compositions of crystal cores. b) Accumulating melt lenses develop gravitational instabilities over timescales of 10-10^2 years (confined case) or up to 10^2-10^3 days (unconfined case). Amalgamation of previously intruded heterogeneous mush pockets with the instability leads to the formation of common rims in crystals. The scale of mush crystal uptake can be limited (crystal-poor Toconao rhyolite) or severe (crystal-rich Atana and Tara dacite). c) Eruptible magma emerges by hybridization of rhyolite melt and pre-existing mush pockets. Residence time of eruptible magma in the crust is on the order of 10-10^3 years.

Acknowledgments

G.W. would like to thank the Swiss National Science Foundation for funding through an Early Postdoc. Mobility Fellowship (project number: P2GEP2 195238). J.B. acknowledges funding from a Royal Society Research Professorship (RP\R1\201048). D.B was funded through a NERC CASE studentship and the European Research Council (ISONEB ERC Adv 321209 & PROCOMM ERC PoC 862389). The authors would like to thank Steve Sparks, Jo Gottsmann, Matt Jackson, David Pyle, Mike Cassidy, and Tamsin Mather for valuable discussion and suggestions regarding various aspects of this work. Tim Elliott is thanked for support of this project and comments that helped to improve the quality of the manuscript. Victoria Smith is acknowledged for support during EPMA analysis at Oxford.

Conflict of Interest

The authors declare that the research was conducted in the absence of any commercial or financial relationships that could be construed as a potential conflict of interest.

Open Research

All data used in this study are available in the electronic supplementary materials to this article and will be uploaded in the *EarthChem* data repository.

References

Allan, A. S. R., Morgan, D. J., Wilson, C. J. N., and Millet, M.-A. (2013). From mush to eruption in centuries: assembly of the super-sized Oruanui magma body. *Contrib Mineral Petrol* 166, 143–164. doi: 10.1007/s00410-013-0869-2.Allan, Aidan. S. R., Barker, S. J., Millet, M.-A., Morgan, D. J., Rooyakkers, S. M., Schipper, C. I., et al. (2017). A cascade of magmatic events during the assembly and eruption of a super-sized magma body. *Contrib Mineral Petrol* 172, 49. doi: 10.1007/s00410-017-1367-8.Andersen, D. J., Lindsley, D. H., and Davidson, P. M. (1993). QUILF: A pascal program to assess equilibria among Fe-Mg-Mn-Ti oxides, pyroxenes, olivine, and quartz. *Computers & Geosciences* 19, 1333–1350. doi: 10.1016/0098-3004(93)90033-2.Annen, C. (2009). From plutons to magma

chambers: Thermal constraints on the accumulation of eruptible silicic magma in the upper crust. *Earth and Planetary Science Letters* 284, 409–416. doi: 10.1016/j.epsl.2009.05.006.Bachmann, O., and Bergantz, G. W. (2004). On the Origin of Crystal-poor Rhyolites: Extracted from Batholithic Crystal Mushes. *Journal of Petrology* 45, 1565–1582. doi: 10.1093/petrology/egh019.Bachmann, O., and Bergantz, G. W. (2006). Gas percolation in upper-crustal silicic crystal mushes as a mechanism for upward heat advection and rejuvenation of near-solidus magma bodies. *Journal of Volcanology and Geothermal Research* 149, 85–102. doi: 10.1016/j.jvolgeores.2005.06.002.Bachmann, O., and Bergantz, G. W. (2008). Rhyolites and their Source Mushes across Tectonic Settings. *Journal of Petrology* 49, 2277–2285. doi: 10.1093/petrology/egn068.Bachmann, O., Dungan, M. A., and Lipman, P. W. (2002). The Fish Canyon Magma Body, San Juan Volcanic Field, Colorado: Rejuvenation and Eruption of an Upper-Crustal Batholith. *Journal of Petrology* 43, 1469–1503. doi: 10.1093/petrology/43.8.1469.Bachmann, O., and Huber, C. (2019). The Inner Workings of Crustal Distillation Columns; the Physical Mechanisms and Rates Controlling Phase Separation in Silicic Magma Reservoirs. *Journal of Petrology* 60, 3–18. doi: 10.1093/petrology/egy103.Barker, S. J., Wilson, C. J. N., Morgan, D. J., and Rowland, J. V. (2016). Rapid priming, accumulation, and recharge of magma driving recent eruptions at a hyperactive caldera volcano. *Geology* 44, 323–326. doi: 10.1130/G37382.1.Bevan, D., D. Coath, C., Lewis, J., Schwieters, J., Lloyd, N., Craig, G., et al. (2021). In situ Rb–Sr dating by collision cell, multicollection inductively-coupled plasma mass-spectrometry with pre-cell mass-filter, (CC-MC-ICPMS/MS). *Journal of Analytical Atomic Spectrometry* 36, 917–931. doi: 10.1039/D1JA00006C.Bindeman, I. N., Davis, A. M., and Drake, M. J. (1998). Ion Microprobe Study of Plagioclase-Basalt Partition Experiments at Natural Concentration Levels of Trace Elements. *Geochimica et Cosmochimica Acta* 62, 1175–1193. doi: 10.1016/S0016-7037(98)00047-7.Black, B. A., Lamarque, J.-F., Marsh, D. R., Schmidt, A., and Bardeen, C. G. (2021). Global climate disruption and regional climate shelters after the Toba supereruption. *Proceedings of the National Academy of Sciences* 118, e2013046118. doi: 10.1073/pnas.2013046118.Brandmeier, M., and Wörner, G. (2016). Compositional variations of ignimbrite magmas in the Central Andes over the past 26 Ma — A multivariate statistical perspective. *Lithos* 262, 713–728. doi: 10.1016/j.lithos.2016.07.011.Burgisser, A., and Bergantz, G. W. (2011). A rapid mechanism to remobilize and homogenize highly crystalline magma bodies. *Nature* 471, 212–215. doi: 10.1038/nature09799.Caricchi, L., Annen, C., Blundy, J., Simpson, G., and Pinel, V. (2014). Frequency and magnitude of volcanic eruptions controlled by magma injection and buoyancy. *Nature Geosci* 7, 126–130. doi: 10.1038/ngeo2041.Caricchi, L., and Blundy, J. (2015). Experimental petrology of monotonous intermediate magmas. *Geological Society, London, Special Publications* 422, 105–130. doi: 10.1144/SP422.9.Cashman, K., and Blundy, J. (2013). Petrological cannibalism: the chemical and textural consequences of incremental magma body growth. *Contrib Mineral Petrol* 166, 703–729. doi: 10.1007/s00410-013-0895-0.Cashman, K. V., Sparks, R. S. J., and Blundy, J. D. (2017). Vertically extensive and unstable magmatic

systems: A unified view of igneous processes. *Science* 355, eaag3055. doi: 10.1126/science.aag3055.Chadwick, J. P., Troll, V. R., Ginibre, C., Morgan, D., Gertisser, R., Waight, T. E., et al. (2007). Carbonate Assimilation at Merapi Volcano, Java, Indonesia: Insights from Crystal Isotope Stratigraphy. *Journal of Petrology* 48, 1793–1812. doi: 10.1093/petrology/egm038.Chamberlain, K. J., Morgan, D. J., and Wilson, C. J. N. (2014). Timescales of mixing and mobilisation in the Bishop Tuff magma body: perspectives from diffusion chronometry. *Contrib Mineral Petrol* 168, 1034. doi: 10.1007/s00410-014-1034-2.Charlier, B. L. A., Bachmann, O., Davidson, J. P., Dungan, M. A., and Morgan, D. J. (2007). The Upper Crustal Evolution of a Large Silicic Magma Body: Evidence from Crystal-scale Rb–Sr Isotopic Heterogeneities in the Fish Canyon Magmatic System, Colorado. *Journal of Petrology* 48, 1875–1894. doi: 10.1093/petrology/egm043.Claiborne, L. L., Miller, C. F., and Wooden, J. L. (2010). Trace element composition of igneous zircon: a thermal and compositional record of the accumulation and evolution of a large silicic batholith, Spirit Mountain, Nevada. *Contrib Mineral Petrol* 160, 511–531. doi: 10.1007/s00410-010-0491-5.Comeau, M. J., Unsworth, M. J., and Cordell, D. (2016). New constraints on the magma distribution and composition beneath Volcán Uturuncu and the southern Bolivian Altiplano from magnetotelluric data. *Geosphere* 12, 1391–1421. doi: 10.1130/GES01277.1.Comeau, M. J., Unsworth, M. J., Ticona, F., and Sunagua, M. (2015). Magnetotelluric images of magma distribution beneath Volcán Uturuncu, Bolivia: Implications for magma dynamics. *Geology* 43, 243–246. doi: 10.1130/G36258.1.Cooper, G. F., Morgan, D. J., and Wilson, C. J. N. (2017). Rapid assembly and rejuvenation of a large silicic magmatic system: Insights from mineral diffusive profiles in the Kidnappers and Rocky Hill deposits, New Zealand. *Earth and Planetary Science Letters* 473, 1–13. doi: 10.1016/j.epsl.2017.05.036.Costa, F., Dohmen, R., and Chakraborty, S. (2008). Time Scales of Magmatic Processes from Modeling the Zoning Patterns of Crystals. *Reviews in Mineralogy and Geochemistry* 69, 545–594. doi: 10.2138/rmg.2008.69.14.Davidson, J. P., Morgan, D. J., Charlier, B. L. A., Harlou, R., and Hora, J. M. (2007). Microsampling and Isotopic Analysis of Igneous Rocks: Implications for the Study of Magmatic Systems. *Annu. Rev. Earth Planet. Sci.* 35, 273–311. doi: 10.1146/annurev.earth.35.031306.140211.Davidson, J., Tepley, F., Palacz, Z., and Meffan-Main, S. (2001). Magma recharge, contamination and residence times revealed by in situ laser ablation isotopic analysis of feldspar in volcanic rocks. *Earth and Planetary Science Letters* 184, 427–442. doi: 10.1016/S0012-821X(00)00333-2.de Silva, S. L. (1989). Geochronology and stratigraphy of the ignimbrites from the 21°30 S to 23°30 S portion of the Central Andes of northern Chile. *Journal of Volcanology and Geothermal Research* 37, 93–131. doi: 10.1016/0377-0273(89)90065-6.de Silva, S. L., and Gosnold, W. D. (2007). Episodic construction of batholiths: Insights from the spatiotemporal development of an ignimbrite flare-up. *Journal of Volcanology and Geothermal Research* 167, 320–335. doi: 10.1016/j.jvolgeores.2007.07.015.de Silva, S. L., and Kay, S. M. (2018). Turning up the Heat: High-Flux Magmatism in the Central Andes. *Elements* 14, 245–250. doi: 10.2138/gselements.14.4.245.De Silva, S., Zandt,

G., Trumbull, R., Viramonte, J. G., Salas, G., and Jiménez, N. (2006). Large ignimbrite eruptions and volcano-tectonic depressions in the Central Andes: a thermomechanical perspective. *Geological Society, London, Special Publications* 269, 47–63. doi: 10.1144/GSL.SP.2006.269.01.04.Del Negro, C., Currenti, G., and Scandura, D. (2009). Temperature-dependent viscoelastic modeling of ground deformation: Application to Etna volcano during the 1993–1997 inflation period. *Physics of the Earth and Planetary Interiors* 172, 299–309. doi: 10.1016/j.pepi.2008.10.019.del Potro, R., Díez, M., Blundy, J., Camacho, A. G., and Gottsmann, J. (2013). Diapiric ascent of silicic magma beneath the Bolivian Altiplano: IGNEOUS DIAPIRS IN THE CENTRAL ANDES. *Geophys. Res. Lett.* 40, 2044–2048. doi: 10.1002/grl.50493.Dohmen, R., Faak, K., and Blundy, J. D. (2017). Chronometry and Speedometry of Magmatic Processes using Chemical Diffusion in Olivine, Plagioclase and Pyroxenes. *Reviews in Mineralogy and Geochemistry* 83, 535–575. doi: 10.2138/rmg.2017.83.16.Druitt, T. H., Costa, F., Deloule, E., Dungan, M., and Scaillet, B. (2012). Decadal to monthly timescales of magma transfer and reservoir growth at a caldera volcano. *Nature* 482, 77–80. doi: 10.1038/nature10706.Dufek, J., and Bachmann, O. (2010). Quantum magmatism: Magmatic compositional gaps generated by melt-crystal dynamics. *Geology* 38, 687–690. doi: 10.1130/G30831.1.Edmonds, M., Cashman, K. V., Holness, M., and Jackson, M. (2019). Architecture and dynamics of magma reservoirs. *Phil. Trans. R. Soc. A.* 377, 20180298. doi: 10.1098/rsta.2018.0298.Farrell, J., Smith, R. B., Husen, S., and Diehl, T. (2014). Tomography from 26 years of seismicity revealing that the spatial extent of the Yellowstone crustal magma reservoir extends well beyond the Yellowstone caldera. *Geophysical Research Letters* 41, 3068–3073. doi: 10.1002/2014GL059588.Freymuth, H., Brandmeier, M., and Wörner, G. (2015). The origin and crust/mantle mass balance of Central Andean ignimbrite magmatism constrained by oxygen and strontium isotopes and erupted volumes. *Contrib Mineral Petrol* 169, 58. doi: 10.1007/s00410-015-1152-5.Gardeweg, M., and Ramírez, C. F. (1987). La Pacana caldera and the Atana Ignimbrite ? a major ash-flow and resurgent caldera complex in the Andes of northern Chile. *Bull Volcanol* 49, 547–566. doi: 10.1007/BF01080449.Ghiorso, M. S. (1984). Activity/composition relations in the ternary feldspars. *Contr. Mineral. and Petrol.* 87, 282–296. doi: 10.1007/BF00373061.Ghiorso, M. S., and Evans, B. W. (2008). Thermodynamics of Rhombohedral Oxide Solid Solutions and a Revision of the FE-TI Two-Oxide Geothermometer and Oxygen-Barometer. *American Journal of Science* 308, 957–1039. doi: 10.2475/09.2008.01.Giletti, B. J., and Casserly, J. E. D. (1994). Strontium diffusion kinetics in plagioclase feldspars. *Geochimica et Cosmochimica Acta* 58, 3785–3793. doi: 10.1016/0016-7037(94)90363-8.Gottsmann, J., Blundy, J., Henderson, S., Pritchard, M. E., and Sparks, R. S. J. (2017). Thermomechanical modeling of the Altiplano-Puna deformation anomaly: Multiparameter insights into magma mush reorganization. *Geosphere*, GES01420.1. doi: 10.1130/GES01420.1.Greco, F., Carbone, D., Cannavò, F., Messina, A. A., and Siligato, G. (2020). "Absolute and Relative Gravity Measurements at Volcanoes: Current State and New Developments Under the NEWTON-g Project," in

International Association of Geodesy Symposia. (Berlin, Heidelberg: Springer), 1–7. doi: 10.1007/1345_2020_126.Grocke, S. B., de Silva, S. L., Iriarte, R., Lindsay, J. M., and Cottrell, E. (2017a). Catastrophic Caldera-Forming (CCF) Monotonous Silicic Magma Reservoirs: Geochemical and Petrological Constraints on Heterogeneity, Magma Dynamics, and Eruption Dynamics of the $3 \cdot 49$ Ma Tara Supereruption, Guacha II Caldera, SW Bolivia. *Journal of Petrology* 58, 227–260. doi: 10.1093/petrology/egx012.Grocke, S. B., de Silva, S. L., Wallace, P. J., Cottrell, E., and Schmitt, A. K. (2017b). Catastrophic Caldera-Forming (CCF) Monotonous Silicic Magma Reservoirs: Constraints from Volatiles in Melt Inclusions from the $3 \cdot 49$ Ma Tara Supereruption, Guacha II Caldera, SW Bolivia. *Journal of Petrology* 58, 2115–2142. doi: 10.1093/petrology/egy003.Gualda, G. A. R., and Sutton, S. R. (2016). The Year Leading to a Supereruption. *PLoS ONE* 11, e0159200. doi: 10.1371/journal.pone.0159200.Hartung, E., Weber, G., and Caricchi, L. (2019). The role of H2O on the extraction of melt from crystallising magmas. *Earth and Planetary Science Letters* 508, 85–96. doi: 10.1016/j.epsl.2018.12.010.Head, M., Hickey, J., Gottsmann, J., and Fournier, N. (2019). The Influence of Viscoelastic Crustal Rheologies on Volcanic Ground Deformation: Insights From Models of Pressure and Volume Change. *Journal of Geophysical Research: Solid Earth* 124, 8127–8146. doi: 10.1029/2019JB017832.Hickey, J., Gottsmann, J., and del Potro, R. (2013). The large-scale surface uplift in the Altiplano-Puna region of Bolivia: A parametric study of source characteristics and crustal rheology using finite element analysis. *Geochemistry, Geophysics, Geosystems* 14, 540–555. doi: 10.1002/ggge.20057.Hickey, J., Gottsmann, J., Nakamichi, H., and Iguchi, M. (2016). Thermomechanical controls on magma supply and volcanic deformation: application to Aira caldera, Japan. *Sci Rep* 6, 32691. doi: 10.1038/srep32691.Holland, T., and Blundy, J. (1994). Non-ideal interactions in calcic amphiboles and their bearing on amphibole-plagioclase thermometry. *Contr. Mineral. and Petrol.* 116, 433–447. doi: 10.1007/BF00310910.Huang, H.-H., Lin, F.-C., Schmandt, B., Farrell, J., Smith, R. B., and Tsai, V. C. (2015). The Yellowstone magmatic system from the mantle plume to the upper crust. *Science* 348, 773–776. doi: 10.1126/science.aaa5648.Huber, C., Bachmann, O., and Dufek, J. (2011). Thermo-mechanical reactivation of locked crystal mushes: Melting-induced internal fracturing and assimilation processes in magmas. *Earth and Planetary Science Letters* 304, 443–454. doi: 10.1016/j.epsl.2011.02.022.Jackson, M. D., Blundy, J., and Sparks, R. S. J. (2018). Chemical differentiation, cold storage and remobilization of magma in the Earth's crust. *Nature* 564, 405–409. doi: 10.1038/s41586-018-0746-2.Jaxybulatov, K., Shapiro, N. M., Koulakov, I., Mordret, A., Landès, M., and Sens-Schönfelder, C. (2014). A large magmatic sill complex beneath the Toba caldera. *Science* 346, 617–619. doi: 10.1126/science.1258582.Kay, S. M., Coira, B. L., Caffe, P. J., and Chen, C.-H. (2010). Regional chemical diversity, crustal and mantle sources and evolution of central Andean Puna plateau ignimbrites. *Journal of Volcanology and Geothermal Research* 198, 81–111. doi: 10.1016/j.jvolgeores.2010.08.013.Kern, J. M., de Silva, S. L., Schmitt, A. K., Kaiser, J. F., Iriarte, A. R., and Economos, R. (2016).

Geochronological imaging of an episodically constructed subvolcanic batholith: U-Pb in zircon chronochemistry of the Altiplano-Puna Volcanic Complex of the Central Andes. *Geosphere* 12, 1054–1077. doi: 10.1130/GES01258.1.Klemetti, E. W., and Clynne, M. A. (2014). Localized Rejuvenation of a Crystal Mush Recorded in Zircon Temporal and Compositional Variation at the Lassen Volcanic Center, Northern California. *PLoS ONE* 9, e113157. doi: 10.1371/journal.pone.0113157.Koulakov, I., Kasatkina, E., Shapiro, N. M., Jaupart, C., Vasilevsky, A., El Khrepy, S., et al. (2016). The feeder system of the Toba supervolcano from the slab to the shallow reservoir. *Nat Commun* 7, 12228. doi: 10.1038/ncomms12228.Lee, C.-T. A., Morton, D. M., Farner, M. J., and Moitra, P. (2015). Field and model constraints on silicic melt segregation by compaction/hindered settling: The role of water and its effect on latent heat release†. *American Mineralogist* 100, 1762–1777. doi: 10.2138/am-2015-5121.Lindsay, J. M. (2001). Magmatic Evolution of the La Pacana Caldera System, Central Andes, Chile: Compositional Variation of Two Cogenetic, Large-Volume Felsic Ignimbrites. *Journal of Petrology* 42, 459–486. doi: 10.1093/petrology/42.3.459.Lindsay, J. M., de Silva, S., Trumbull, R., Emmermann, R., and Wemmer, K. (2001). La Pacana caldera, N. Chile: a re-evaluation of the stratigraphy and volcanology of one of the world's largest resurgent calderas. *Journal of Volcanology and Geothermal Research* 106, 145–173. doi: 10.1016/S0377-0273(00)00270-5.Liu, M., and Yund, R. A. (1992). NaSi-CaAl interdiffusion in plagioclase. *American Mineralogist* 77, 275–283.Liu, P.-P., Caricchi, L., Chung, S.-L., Li, X.-H., Li, Q.-L., Zhou, M.-F., et al. (2021). Growth and thermal maturation of the Toba magma reservoir. *PNAS* 118. doi: 10.1073/pnas.2101695118.Lowenstern, J., Sisson, T., and Hurwitz, S. (2017). Probing Magma Reservoirs to Improve Volcano Forecasts. *Eos*. doi: 10.1029/2017EO085189.Lukács, R., Caricchi, L., Schmitt, A. K., Bachmann, O., Karakas, O., Guillong, M., et al. (2021). Zircon geochronology suggests a long-living and active magmatic system beneath the Ciomadul volcanic dome field (eastern-central Europe). *Earth and Planetary Science Letters* 565, 116965. doi: 10.1016/j.epsl.2021.116965.Magee, C., Stevenson, C. T. E., Ebmeier, S. K., Keir, D., Hammond, J. O. S., Gottsmann, J. H., et al. (2018). Magma Plumbing Systems: A Geophysical Perspective. *Journal of Petrology* 59, 1217–1251. doi: 10.1093/petrology/egy064.Marsh, B. D. (1981). On the crystallinity, probability of occurrence, and rheology of lava and magma. *Contr. Mineral. and Petrol.* 78, 85–98. doi: 10.1007/BF00371146.McKenzie, D. (1985). The extraction of magma from the crust and mantle. *Earth and Planetary Science Letters* 74, 81–91.McNutt, S. R. (1996). "Seismic Monitoring and Eruption Forecasting of Volcanoes: A Review of the State-of-the-Art and Case Histories," in *Monitoring and Mitigation of Volcano Hazards*, eds. R. Scarpa and R. I. Tilling (Berlin, Heidelberg: Springer), 99–146. doi: 10.1007/978-3-642-80087-0_3.Morales Rivera, A. M., Amelung, F., Albino, F., and Gregg, P. M. (2019). Impact of Crustal Rheology on Temperature-Dependent Viscoelastic Models of Volcano Deformation: Application to Taal Volcano, Philippines. *Journal of Geophysical Research: Solid Earth* 124, 978–994. doi: 10.1029/2018JB016054.Papale, P.

(2018). Global time-size distribution of volcanic eruptions on Earth. *Sci Rep* 8, 6838. doi: 10.1038/s41598-018-25286-y.Perez, W. A., and Dunn, T. (1996). Diffusivity of strontium, neodymium, and lead in natural rhyolite melt at 1.0 GPa. *Geochimica et Cosmochimica Acta* 60, 1387–1397. doi: 10.1016/0016-7037(96)00016-6.Perkins, J. P., Ward, K. M., de Silva, S. L., Zandt, G., Beck, S. L., and Finnegan, N. J. (2016). Surface uplift in the Central Andes driven by growth of the Altiplano Puna Magma Body. *Nat Commun* 7, 13185. doi: 10.1038/ncomms13185.Pistone, M., Blundy, J., and Brooker, R. A. (2017). Water transfer during magma mixing events: Insights into crystal mush rejuvenation and melt extraction processes. *American Mineralogist* 102, 766–776. doi: 10.2138/am-2017-5793.Poland, M. P., and Zebker, H. A. (2022). Volcano geodesy using InSAR in 2020: the past and next decades. *Bull Volcanol* 84, 27. doi: 10.1007/s00445-022-01531-1.Pritchard, M. E., de Silva, S. L., Michelfelder, G., Zandt, G., McNutt, S. R., Gottsmann, J., et al. (2018). Synthesis: PLUTONS: Investigating the relationship between pluton growth and volcanism in the Central Andes. *Geosphere* 14, 954–982. doi: 10.1130/GES01578.1.Putirka, K. D. (2005). Igneous thermometers and barometers based on plagioclase + liquid equilibria: Tests of some existing models and new calibrations. *American Mineralogist* 90, 336–346. doi: 10.2138/am.2005.1449.Ramos, F. C., Wolff, J. A., and Tollstrup, D. L. (2005). Sr isotope disequilibrium in Columbia River flood basalts: Evidence for rapid shallow-level open-system processes. *Geology* 33, 457–460. doi: 10.1130/G21512.1.Rampino, M. R. (2002). Supereruptions as a Threat to Civilizations on Earth-like Planets. *Icarus* 156, 562–569. doi: 10.1006/icar.2001.6808.Rubin, A. E., Cooper, K. M., Till, C. B., Kent, A. J. R., Costa, F., Bose, M., et al. (2017). Rapid cooling and cold storage in a silicic magma reservoir recorded in individual crystals. *Science* 356, 1154–1156. doi: 10.1126/science.aam8720.Russell, W. A., Papanastassiou, D. A., and Tombrello, T. A. (1978). Ca isotope fractionation on the Earth and other solar system materials. *Geochimica et Cosmochimica Acta* 42, 1075–1090. doi: 10.1016/0016-7037(78)90105-9.Salisbury, M. J., Jicha, B. R., de Silva, S. L., Singer, B. S., Jimenez, N. C., and Ort, M. H. (2011). 40Ar/39Ar chronostratigraphy of Altiplano-Puna volcanic complex ignimbrites reveals the development of a major magmatic province. *Geological Society of America Bulletin* 123, 821–840. doi: 10.1130/B30280.1.Schmitt, A., de Silva, S., Trumbull, R., and Emmermann, R. (2001). Magma evolution in the Purico ignimbrite complex, northern Chile: evidence for zoning of a dacitic magma by injection of rhyolitic melts following mafic recharge. *Contrib Mineral Petrol* 140, 680–700. doi: 10.1007/s004100000214.Self, S. (2006). The effects and consequences of very large explosive volcanic eruptions. *Phil. Trans. R. Soc. A.* 364, 2073–2097. doi: 10.1098/rsta.2006.1814.Self, S., and Blake, S. (2008). Consequences of Explosive Supereruptions. *Elements* 4, 41–46. doi: 10.2113/GSELEMENTS.4.1.41.Seropian, G., Rust, A. C., and Sparks, R. S. J. (2018). The Gravitational Stability of Lenses in Magma Mushes: Confined Rayleigh-Taylor Instabilities. *J. Geophys. Res. Solid Earth* 123, 3593–3607. doi: 10.1029/2018JB015523.Shamloo, H. I., and Till, C. B. (2019). Decadal transition from quiescence to supereruption: petrologic

investigation of the Lava Creek Tuff, Yellowstone Caldera, WY. *Contrib Mineral Petrol* 174, 32. doi: 10.1007/s00410-019-1570-x.Sisson, T. W., and Bacon, C. R. (1999). Gas-driven filter pressing in magmas. *Geol* 27, 613. doi: 10.1130/0091-7613(1999)027<0613:GDFPIM>2.3.CO;2.Sliwinski, J., Farsky, D., Lipman, P. W., Guillong, M., and Bachmann, O. (2019). Rapid Magma Generation or Shared Magmatic Reservoir? Petrology and Geochronology of the Rat Creek and Nelson Mountain Tuffs, CO, USA. *Front. Earth Sci.* 7, 271. doi: 10.3389/feart.2019.00271.Solano, J. M. S., Jackson, M. D., Sparks, R. S. J., and Blundy, J. (2014). Evolution of major and trace element composition during melt migration through crystalline mush: Implications for chemical differentiation in the crust. *American Journal of Science* 314, 895–939. doi: 10.2475/05.2014.01.Solano, J. M. S., Jackson, M. D., Sparks, R. S. J., Blundy, J. D., and Annen, C. (2012). Melt Segregation in Deep Crustal Hot Zones: a Mechanism for Chemical Differentiation, Crustal Assimilation and the Formation of Evolved Magmas. *Journal of Petrology* 53, 1999–2026. doi: 10.1093/petrology/egs041.Sparks, R. S. J., Annen, C., Blundy, J. D., Cashman, K. V., Rust, A. C., and Jackson, M. D. (2019). Formation and dynamics of magma reservoirs. *Phil. Trans. R. Soc. A.* 377, 20180019. doi: 10.1098/rsta.2018.0019.Sparks, R. S. J., Blundy, J. D., Cashman, K. V., Jackson, M., Rust, A., and Wilson, C. J. N. (2022). Large silicic magma bodies and very large magnitude explosive eruptions. *Bull Volcanol* 84, 8. doi: 10.1007/s00445-021-01510-y.Spera, F. J., and Bohrson, W. A. (2018). Rejuvenation of crustal magma mush: A tale of multiply nested processes and timescales. *Am J Sci* 318, 90–140. doi: 10.2475/01.2018.05.Szymanowski, D., Ellis, B. S., Wotzlaw, J.-F., and Bachmann, O. (2019). Maturation and rejuvenation of a silicic magma reservoir: High-resolution chronology of the Kneeling Nun Tuff. *Earth and Planetary Science Letters* 510, 103–115. doi: 10.1016/j.epsl.2019.01.007.Szymanowski, D., Wotzlaw, J.-F., Ellis, B. S., Bachmann, O., Guillong, M., and von Quadt, A. (2017). Protracted near-solidus storage and pre-eruptive rejuvenation of large magma reservoirs. *Nature Geosci* 10, 777–782. doi: 10.1038/ngeo3020.Tapster, S., Condon, D. J., Naden, J., Noble, S. R., Petterson, M. G., Roberts, N. M. W., et al. (2016). Rapid thermal rejuvenation of high-crystallinity magma linked to porphyry copper deposit formation; evidence from the Koloula Porphyry Prospect, Solomon Islands. *Earth and Planetary Science Letters* 442, 206–217. doi: 10.1016/j.epsl.2016.02.046.Telford, W. M., Telford, W. M., Geldart, L. P., and Sheriff, R. E. (1990). *Applied Geophysics*. Cambridge University Press.Tepley, F. J., Davidson, J. P., Tilling, R. I., and Arth, J. G. (2000). Magma Mixing, Recharge and Eruption Histories Recorded in Plagioclase Phenocrysts from El Chichón Volcano, Mexico. *Journal of Petrology* 41, 1397–1411. doi: 10.1093/petrology/41.9.1397.Townsend, M. (2022). Linking surface deformation to thermal and mechanical magma chamber processes. *Earth and Planetary Science Letters* 577, 117272. doi: 10.1016/j.epsl.2021.117272.Trasatti, E., Acocella, V., Di Vito, M. A., Del Gaudio, C., Weber, G., Aquino, I., et al. (2019). Magma Degassing as a Source of Long-Term Seismicity at Volcanoes: The Ischia Island (Italy) Case. *Geophys. Res. Lett.* 46, 14421–14429. doi:

10.1029/2019GL085371.van Zalinge, M. E., Cashman, K. V., and Sparks, R. S. J. (2018). Causes of fragmented crystals in ignimbrites: a case study of the Cardones ignimbrite, Northern Chile. *Bull Volcanol* 80, 22. doi: 10.1007/s00445-018-1196-2.van Zalinge, M. E., Mark, D. F., Sparks, R. S. J., Tremblay, M. M., Keller, C. B., Cooper, F. J., et al. (2022). Timescales for pluton growth, magma-chamber formation and super-eruptions. *Nature* 608, 87–92. doi: 10.1038/s41586-022-04921-9.Vigneresse, J. L., Barbey, P., and Cuney, M. (1996). Rheological Transitions During Partial Melting and Crystallization with Application to Felsic Magma Segregation and Transfer. *Journal of Petrology* 37, 1579–1600. doi: 10.1093/petrology/37.6.1579.Villa, I. M., De Bièvre, P., Holden, N. E., and Renne, P. R. (2015). IUPAC-IUGS recommendation on the half life of 87Rb. *Geochimica et Cosmochimica Acta* 164, 382–385. doi: 10.1016/j.gca.2015.05.025.Waight, T. E., and Tørnqvist, J. B. (2018). Sr isotope zoning in plagioclase from andesites at Cabo De Gata, Spain: Evidence for shallow and deep contamination. *Lithos* 308–309, 159–167. doi: 10.1016/j.lithos.2018.03.007.Ward, K. M., Delph, J. R., Zandt, G., Beck, S. L., and Ducea, M. N. (2017). Magmatic evolution of a Cordilleran flare-up and its role in the creation of silicic crust. *Sci Rep* 7, 9047. doi: 10.1038/s41598-017-09015-5.Ward, K. M., Zandt, G., Beck, S. L., Christensen, D. H., and McFarlin, H. (2014). Seismic imaging of the magmatic underpinnings beneath the Altiplano-Puna volcanic complex from the joint inversion of surface wave dispersion and receiver functions. *Earth and Planetary Science Letters* 404, 43–53. doi: 10.1016/j.epsl.2014.07.022.Waters, L. E., and Lange, R. A. (2015). An updated calibration of the plagioclase-liquid hygrometer-thermometer applicable to basalts through rhyolites. *American Mineralogist* 100, 2172–2184. doi: 10.2138/am-2015-5232.Weber, G., Arce, J. L., Ulianov, A., and Caricchi, L. (2019). A Recurrent Magmatic Pattern on Observable Timescales Prior to Plinian Eruptions From Nevado de Toluca (Mexico). *J. Geophys. Res. Solid Earth* 124, 10999–11021. doi: 10.1029/2019JB017640.Weber, G., Caricchi, L., Arce, J. L., and Schmitt, A. K. (2020a). Determining the current size and state of subvolcanic magma reservoirs. *Nat Commun* 11, 5477. doi: 10.1038/s41467-020-19084-2.Weber, G., and Castro, J. M. (2017). Phase petrology reveals shallow magma storage prior to large explosive silicic eruptions at Hekla volcano, Iceland. *Earth and Planetary Science Letters* 466, 168–180. doi: 10.1016/j.epsl.2017.03.015.Weber, G., Simpson, G., and Caricchi, L. (2020b). Magma diversity reflects recharge regime and thermal structure of the crust. *Sci Rep* 10, 11867. doi: 10.1038/s41598-020-68610-1.Whitehead Jr, J. A., and Luther, D. S. (1975). Dynamics of laboratory diapir and plume models. *Journal of Geophysical Research* 80, 705–717.Wilke, M., and Behrens, H. (1999). The dependence of the partitioning of iron and europium between plagioclase and hydrous tonalitic melt on oxygen fugacity. *Contributions to Mineralogy and Petrology* 137, 102–114. doi: 10.1007/s004100050585.Wilson, C. J. N., Cooper, G. F., Chamberlain, K. J., Barker, S. J., Myers, M. L., Illsley-Kemp, F., et al. (2021). No single model for supersized eruptions and their magma bodies. *Nat Rev Earth Environ* 2, 610–627. doi: 10.1038/s43017-021-00191-7.Wotzlaw, J.-F., Bindeman, I. N., Watts, K. E., Schmitt, A. K., Caricchi, L., and

Schaltegger, U. (2014). Linking rapid magma reservoir assembly and eruption trigger mechanisms at evolved Yellowstone-type supervolcanoes. *Geology* 42, 807–810. doi: 10.1130/G35979.1.Wotzlaw, J.-F., Schaltegger, U., Frick, D. A., Dungan, M. A., Gerdes, A., and Günther, D. (2013). Tracking the evolution of large-volume silicic magma reservoirs from assembly to supereruption. *Geology* 41, 867–870. doi: 10.1130/G34366.1.Zandt, G., Leidig, M., Chmielowski, J., Baumont, D., and Yuan, X. (2003). Seismic Detection and Characterization of the Altiplano-Puna Magma Body, Central Andes. *Pure appl. geophys.* 160, 789–807. doi: 10.1007/PL00012557.